# Refining Generative Process with Discriminator Guidance in Score-based Diffusion Models

Dongjun Kim<sup>\*1</sup> Yeongmin Kim<sup>\*1</sup> Se Jung Kwon<sup>2</sup> Wanmo Kang<sup>1</sup> Il-Chul Moon<sup>1</sup>

## **Abstract**

While there are many score-based models with various diffusing strategies as well as many numerical schemes of the denoising process, only a few works have explored the score part of the generative SDE. This paper introduces a new generative SDE with score adjustment using an auxiliary discriminator. The goal is to improve the original generative process of a pre-trained diffusion model by estimating the gap between the pretrained score estimation and the true data score. This is done by training a discriminator that classifies diffused real data and diffused sample data. The gap estimation is then used to adjust the pretrained score network. In experiments, the method enables new SOTA FIDs of 1.77/1.64 on unconditional/conditional CIFAR-10, and new SOTA FID/sFID of 3.18/4.53 on ImageNet 256x256.

## 1. Introduction

The diffusion model has recently been highlighted for its success in image generation (Dhariwal & Nichol, 2021; Ho et al., 2021; Karras et al., 2022; Song et al., 2020b), video

generation (Singer et al., 2022; Ho et al., 2022; Voleti et al., 2022), and text-to-image generation (Rombach et al., 2022; Ramesh et al., 2022; Saharia et al., 2022). The State-Of-The-Art (SOTA) models perform human-level generation, but there is still much more room to be investigated for a deep understanding on diffusion models.

The generative model community shares well-trained score models (Dhariwal & Nichol, 2021; Rombach et al., 2022), which are widely used in downstream tasks (Meng et al., 2021; Kawar et al., 2022; Su et al., 2022; Kim et al.) because 1) the estimation target of diffusion models is fixed as a data score across diffusion models, and 2) training a new model is computationally expensive. However, most of the previous research on CIFAR-10 saturates at Fréchet Inception Distance (FID) near 2.20 (Song et al., 2020b), and no significant improvement is made by further training pretrained score networks, varying diffusion strategies (Karras et al., 2022; Dockhorn et al., 2022), or integrating diverse network structures (Vahdat et al., 2021; Kim et al., 2022b).

This paper introduces an orthogonal approach to improve sample quality of a given pre-trained score network. We directly quantify the gap between the pre-trained score estimation and the true data score, and we estimate this gap by an auxiliary discriminator network. The discriminator provides an additional degree of freedom to the diffusion model, and we prove that the discriminator effectively finds meaningful information that is not captured by score training. We construct the adjusted score by summing the estimated

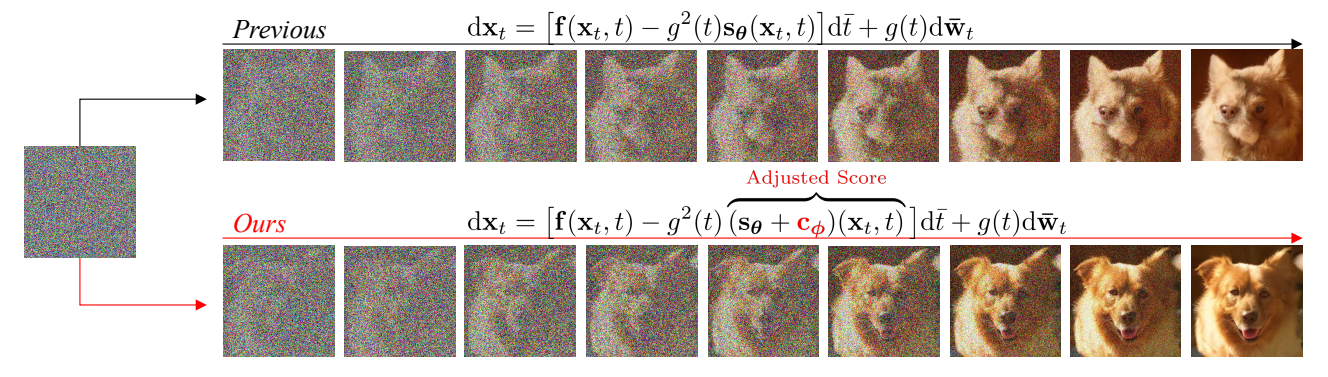


Figure 1: Comparison of the denoising processes. The discriminator guidance estimates the gap by  $c_{\phi}$  with a neural discriminator, where the adjusted score coincides the data score at the optimal discriminator.

<sup>\*</sup>Equal contribution <sup>1</sup>Department of Industrial and Systems Engineering, KAIST, South Korea <sup>2</sup>NAVER Cloud, South Korea. Correspondence to: Dongjun Kim <dongjoun57@kaist.ac.kr>.



Figure 2: Samples from ImageNet 256x256 with (a) ADM, (b) ADM with classifier guidance, and (c) ADM with classifier + discriminator guidance. ADM-G++ is as diverse as ADM and as realistic as ADM-G, see Appendix D.3 for more samples.

gap to the pre-trained score estimation, and this adjustment achieves new SOTA performances on CIFAR-10, CelebA, FFHQ, and ImageNet 256x256. The discriminator saturates very fast (within 10 epochs), so such a significant performance boost could be achieved by cheap budget. We summarize the contributions as follows.

- ✓ We propose a new generative process, Discriminator Guidance, with an adjusted score of a given pretrained score model.
- √ We show that the discriminator-guided samples are closer to the real-world data than the non-guided samples, theoretically and empirically.

## 2. Preliminary and Related Works

The forward-time diffusion process perturbs the data variable into a noise variable by adding iterative Gaussian noises (Ho et al., 2020; Dhariwal & Nichol, 2021), i.e.,

$$\mathbf{x}_{t+1} = \sqrt{1 - \beta_t} \mathbf{x}_t + \beta_t \boldsymbol{\epsilon}_t,$$

where  $\epsilon_t$  follows a standard Gaussian distribution  $\mathcal{N}(0, \mathbf{I})$ , t is a time index for intermediate perturbation, and  $\beta_t$  determines the perturbing speed. In its continuous limit (Song

et al., 2020b), this diffusion process can be maximally generalized as a stochastic differential equation (SDE) of

$$d\mathbf{x}_t = \mathbf{f}(\mathbf{x}_t, t) dt + g(t) d\mathbf{w}_t, \tag{1}$$

with t being a continuum of the diffusion index in [0,T], and  $\mathbf{f}(\mathbf{x}_t,t)$  and g(t) being the drift and the volatility coefficients, respectively. We describe our model under the continuous-time framework mainly for the purpose of notational simplicity. Our model is applicable to both discrete-and continuous-time settings.

The forward SDE of Eq. (1) has a unique reverse-time diffusion process

$$d\mathbf{x}_t = \left[ \mathbf{f}(\mathbf{x}_t, t) - g^2(t) \nabla \log p_r^t(\mathbf{x}_t) \right] d\bar{t} + g(t) d\bar{\mathbf{w}}_t, (2)$$

where  $\mathrm{d}\bar{t}$  and  $\bar{\mathbf{w}}_t$  are the infinitesimal reverse-time and the reverse-time Brownian motion, respectively. The solution of this reverse SDE matches that of the forward SDE if the marginal densities at initial and final time are identical.

The diffusion model trains a score network  $\mathbf{s}_{\theta}$  to estimate the intractable data score  $\nabla \log p_r^t(\mathbf{x}_t)$  with an objective

$$\mathcal{L}_{\boldsymbol{\theta}} = \frac{1}{2} \int_{0}^{T} \xi(t) \mathbb{E} \left[ \| \mathbf{s}_{\boldsymbol{\theta}}(\mathbf{x}_{t}, t) - \nabla \log p_{r}^{t}(\mathbf{x}_{t}) \|_{2}^{2} \right] dt, \quad (3)$$

### **Algorithm 1** Discriminator Training

- 1: Construct  $\mathcal{D} = \{\mathbf{x}_1, ..., \mathbf{x}_M\}$  from the real-world
- 2: Construct  $\mathcal{G} = \{\hat{\mathbf{x}}_1, ..., \hat{\mathbf{x}}_N\}$  by sampling from  $p_{\theta}$
- while converged do
- 4: Sample  $\mathbf{x}_1, ..., \mathbf{x}_{B/2}$  from the real dataset  $\mathcal{D}$
- 5: Sample  $\mathbf{x}_{B/2+1},...,\mathbf{x}_{B}$  from the sample dataset  $\mathcal{G}$
- Sample  $t_1, ..., t_B$  from [0, T]6:
- $\text{Diffuse } \mathbf{x}_i^{t_i} \leftarrow e^{-\int_0^{t_i} \beta_s \, \mathrm{d}s} \mathbf{x}_i + \sqrt{1 e^{-\int_0^{t_i} \beta_s} \, \mathrm{d}s} \boldsymbol{\epsilon}_i$
- for  $\epsilon_i \sim \mathcal{N}(0, \mathbf{I}), \forall i = 1, ..., B$ Calculate  $\hat{\mathcal{L}}_{\phi} \leftarrow -\sum_{i=1}^{B/2} \lambda(t_i) \log d_{\phi}(\mathbf{x}_i^{t_i}, t_i)$  $\sum_{i=B/2+1}^{B} \lambda(t_i) \log \left(1 - d_{\boldsymbol{\phi}}(\mathbf{x}_i^{t_i}, t_i)\right)$
- Update  $\phi \leftarrow \phi \frac{\partial \hat{\mathcal{L}}_{\phi}}{\partial \phi}$
- 10: end while

where  $\xi$  is the temporal weight and  $p_r^t$  is the marginal density of the data forward diffusion of Eq. (1). This objective function is equivalently interpretable as the noise estimation  $\sum \mathbb{E}[\|\epsilon_{\theta} - \epsilon\|_2^2]$  (Ho et al., 2020) or the data reconstruction  $\sum \mathbb{E}[\|\hat{\mathbf{x}}_{\boldsymbol{\theta}}(\mathbf{x}_t) - \mathbf{x}_0\|_2^2]$  (Kingma et al., 2021).

There are various choices for perturbation strategies. The Variance Exploding (VE) SDEs (Song et al., 2020b) of  $d\mathbf{x}_t = g(t) d\mathbf{w}_t$  has a solution  $\mathbf{x}_t \sim \mathcal{N}(\mathbf{x}_0, \sigma^2(t)\mathbf{I})$ , where  $\sigma(t)$  is subordinate to g(t). The Variance Preserving (VP) SDEs (Ho et al., 2020) are defined as a special case of Ornstein-Uhlenbeck process (Särkkä & Solin, 2019) with nonzero drift term. Mathematically, all VE/VP SDEs are equivalent under scale translations, so we interchangeably denote  $x_t$  and  $x_{\sigma}$  if no confusion arises. The point, however, is that the equivalent variations show different performances in empirical studies, and it is far-reaching to understand the behavioral differences (Kim et al., 2022a).

## 3. Refining Generative Process with Discriminator Guidance

#### 3.1. Correction of Pre-trained Score Estimation

After score training, we synthesize samples from the timereversal generative process

$$d\mathbf{x}_{t} = \left[\mathbf{f}(\mathbf{x}_{t}, t) - g^{2}(t)\mathbf{s}_{\boldsymbol{\theta}_{\infty}}(\mathbf{x}_{t}, t)\right] d\bar{t} + g(t) d\bar{\mathbf{w}}_{t}, \quad (4)$$

where  $\mathbf{s}_{\boldsymbol{\theta}_{\infty}}$  represents the score network after the convergence. This generative process could differ from the reversetime data process if  $\theta_{\infty}$  deviates from the global optimum  $\theta_*$ . We show in Theorem 1 that the generative process of Eq. (4) coincides with the reverse-time data process of Eq. (2) if we adjust the score estimation. We call this gap by the correction term, which is nonzero as long as  $\theta_{\infty} \neq \theta_{*}$ .

**Theorem 1.** Suppose  $p_{\theta_{\infty}}$  be the solution of the timereversal generative process of Eq. (4). Let  $p_r^t$  and  $p_{\theta}^t$ . be the marginal densities (at t) of the forward-time SDE

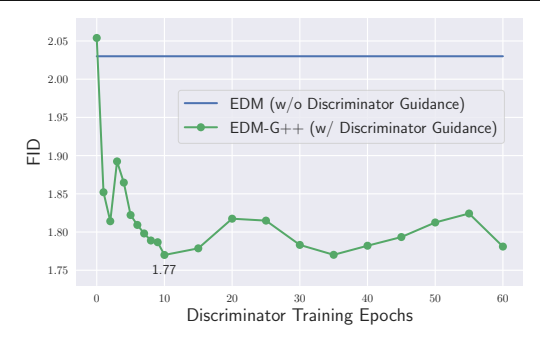


Figure 3: Discriminator guidance refines FID on CIFAR-10.

 $d\mathbf{x}_t = \mathbf{f}(\mathbf{x}_t, t) dt + g(t) d\mathbf{w}_t$  starting from  $p_r$  and  $p_{\theta_{\infty}}$ , respectively. If  $\mathbf{s}_{\theta_{\infty}}(\mathbf{x}, T) = \nabla \log \pi(\mathbf{x})$ , where  $\pi$  is the prior distribution, and the log-likelihood  $\log p_{\theta_{\infty}}$  equals its evidence lower bound  $\mathcal{L}_{\theta_{\infty}}$ , then the reverse-time SDE

$$d\mathbf{x}_t = \left[ \mathbf{f}(\mathbf{x}_t, t) - g^2(t) \nabla \log p_r^t(\mathbf{x}_t) \right] d\bar{t} + g(t) d\bar{\mathbf{w}}_t,$$

coincides with a diffusion process with adjusted score,

$$d\mathbf{x}_{t} = \left[\mathbf{f}(\mathbf{x}_{t}, t) - g^{2}(t)(\mathbf{s}_{\boldsymbol{\theta}_{\infty}} + \mathbf{c}_{\boldsymbol{\theta}_{\infty}})(\mathbf{x}_{t}, t)\right] d\bar{t} + g(t) d\bar{\mathbf{w}}_{t},$$

$$for \, \mathbf{c}_{\boldsymbol{\theta}_{\infty}}(\mathbf{x}_{t}, t) := \nabla \log \frac{p_{r}^{t}(\mathbf{x}_{t})}{p_{\boldsymbol{\theta}_{\infty}}^{t}(\mathbf{x}_{t})}.$$

#### 3.2. Discriminator Guidance

The correction term  $\mathbf{c}_{\boldsymbol{\theta}_{\infty}}(\mathbf{x}_t,t)$  is intractable in general because the density-ratio  $\frac{p_r^t}{p_{\theta,\infty}^t}$  is inaccessible. Therefore, we estimate this density-ratio by training a discriminator with an additional argument of diffusion time t. For discriminator training, we use the Binary Cross Entropy (BCE)

$$\mathcal{L}_{\phi} = \int \lambda(t) \left( \mathbb{E}_{p_r^t(\mathbf{x}_t)} [-\log d_{\phi}(\mathbf{x}_t, t)] + \mathbb{E}_{p_{\theta_{\infty}}^t(\mathbf{x}_t)} [-\log (1 - d_{\phi}(\mathbf{x}_t, t))] \right) dt,$$
(5)

where  $\lambda$  is the temporal weight. The discriminator classifies diffused real data  $\mathbf{x}_t \sim p_r^t$  as real and diffused sample data  $\mathbf{x}_t \sim p_{\boldsymbol{\theta}_{\infty}}^t$  as fake, see Algorithm 1 and Appendix A.4 for details. Then, as the correction term is represented as

$$\mathbf{c}_{\boldsymbol{\theta}_{\infty}}(\mathbf{x}_{t}, t) = \nabla \log \frac{d_{\boldsymbol{\phi}_{*}}(\mathbf{x}_{t}, t)}{1 - d_{\boldsymbol{\phi}_{*}}(\mathbf{x}_{t}, t)}$$

in terms of the optimal discriminator  $d_{\phi_*}$  of  $\mathcal{L}_{\phi}$ , we estimate the correction term  $\mathbf{c}_{m{ heta}_{\infty}}$  with a neural discriminator  $d_{m{\phi}}$  by

$$\mathbf{c}_{\boldsymbol{\theta}_{\infty}}(\mathbf{x}_{t}, t) \approx \mathbf{c}_{\boldsymbol{\phi}}(\mathbf{x}_{t}, t) := \nabla \log \frac{d_{\boldsymbol{\phi}}(\mathbf{x}_{t}, t)}{1 - d_{\boldsymbol{\phi}}(\mathbf{x}_{t}, t)}$$

With the above tractable correction estimate, we define the **Discriminator Guidance** (DG) by

$$d\mathbf{x}_{t} = \left[\mathbf{f}(\mathbf{x}_{t}, t) - g^{2}(t)(\mathbf{s}_{\boldsymbol{\theta}_{\infty}} + \mathbf{c}_{\boldsymbol{\phi}})(\mathbf{x}_{t}, t)\right] d\bar{t} + g(t) d\bar{\mathbf{w}}_{t}.$$
(6)

Figure 3 shows that the discriminator indeed improves sample quality with a quick convergence: as the discriminator training matures, FID improves.

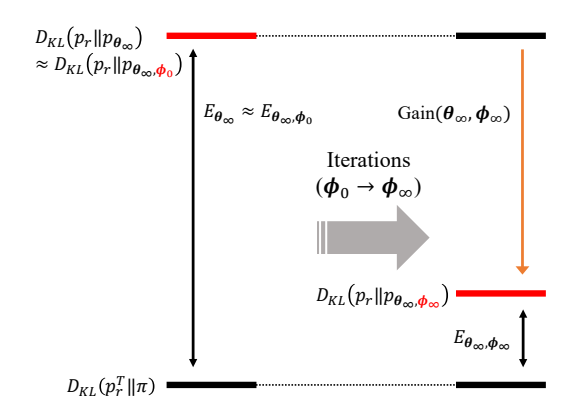


Figure 4: Schematic illustration of the analysis in Section 3.3. The gain increases as discriminator learns.

## 3.3. Theoretical Analysis

In spite that we stated the discriminator guidance in view of differential equations, this section treats the distributional discrepancy between the sample distribution and the data distribution. Let  $p_{\theta_{\infty},\phi}$  to be the sample distribution of the discriminator guidance in Eq. (6). Then, the question is

Is  $p_{\theta_{\infty}, \phi}$  closer to the data distribution  $p_r$  than  $p_{\theta_{\infty}}$ ?

We answer the question in Theorem 2. See Appendix A for details.

**Theorem 2.** If the assumptions of Theorem 1 hold, then

$$D_{KL}(p_r || p_{\boldsymbol{\theta}_{\infty}}) = D_{KL}(p_r^T || \pi) + E_{\boldsymbol{\theta}_{\infty}},$$
  
$$D_{KL}(p_r || p_{\boldsymbol{\theta}_{\infty}, \boldsymbol{\phi}}) \le D_{KL}(p_r^T || \pi) + E_{\boldsymbol{\theta}_{\infty}, \boldsymbol{\phi}},$$

where

$$E_{\boldsymbol{\theta}_{\infty}} = \frac{1}{2} \int_{0}^{T} g^{2}(t) \mathbb{E}_{p_{r}^{t}} \left[ \|\nabla \log p_{r}^{t} - \mathbf{s}_{\boldsymbol{\theta}_{\infty}}\|_{2}^{2} \right],$$

$$E_{\boldsymbol{\theta}_{\infty}, \boldsymbol{\phi}} = \frac{1}{2} \int_{0}^{T} g^{2}(t) \mathbb{E}_{p_{r}^{t}} \left[ \|\nabla \log p_{r}^{t} - (\mathbf{s}_{\boldsymbol{\theta}_{\infty}} + \mathbf{c}_{\boldsymbol{\phi}})\|_{2}^{2} \right] dt$$

$$= \frac{1}{2} \int_{0}^{T} g^{2}(t) \mathbb{E}_{p_{r}^{t}} \left[ \|\mathbf{c}_{\boldsymbol{\theta}_{\infty}} - \mathbf{c}_{\boldsymbol{\phi}}\|_{2}^{2} \right] dt.$$

By subtracting two KL divergences in Theorem 2, we could quantize the gain of discriminator training by

$$D_{KL}(p_r || p_{\boldsymbol{\theta}_{\infty}, \boldsymbol{\phi}}) \leq D_{KL}(p_r || p_{\boldsymbol{\theta}_{\infty}}) - \operatorname{Gain}(\boldsymbol{\theta}_{\infty}, \boldsymbol{\phi}),$$

where  $\mathrm{Gain}(\theta_\infty,\phi)=E_{\theta_\infty}-E_{\theta_\infty,\phi}$ . If the discriminator is blind  $(d_{\phi_b}\equiv 0.5)$ , then the discriminator error  $E_{\theta_\infty,\phi_b}$  equals the score error  $E_{\theta_\infty}$ . Thus, the gain is approximately zero when the discriminator is untrained  $(d_{\phi_0}\approx 0.5)$ . The optimal discriminator satisfies  $E_{\theta_\infty,\phi_*}=0$ , so the gain is maximized as discriminator updates its parameters.

In other words, we interpret that the discriminator guidance reparametrizes the score error  $E_{\theta_{\infty}}$  with a discriminator

Algorithm 2 Sampling with Guidance Techniques

1: Sample 
$$\mathbf{x}_{T} \sim \mathcal{N}(0, \sigma_{max}^{2}\mathbf{I})$$
2:  $\mathbf{for}\ i = N\ \text{to}\ 1\ \mathbf{do}$ 
3: Sample  $\boldsymbol{\epsilon}_{i} \sim \mathcal{N}(0, S_{1}^{2}\mathbf{I})\ \text{and}\ \boldsymbol{\epsilon}_{i}' \sim \mathcal{N}(0, \mathbf{I})$ 
4:  $\hat{t}_{i} \leftarrow \sigma^{-1}((1 + \gamma_{t_{i}})\sigma(t_{i}))\ (\mathbf{Karras}\ \text{et}\ \text{al.}, 2022)$ 
5:  $\mathbf{x}_{\hat{t}_{i}} \leftarrow \mathbf{x}_{t_{i}} + \sqrt{\sigma^{2}(\hat{t}_{i}) - \sigma^{2}(t_{i})}\boldsymbol{\epsilon}_{t_{i}}$ 
6:  $\mathbf{s}_{\hat{t}_{i}} \leftarrow \mathbf{f}(\mathbf{x}_{\hat{t}_{i}}, \hat{t}_{i}) - \frac{1+\eta^{2}}{2}g_{\hat{t}_{i}}^{2}\mathbf{s}_{\boldsymbol{\theta}_{\infty}}(\mathbf{x}_{\hat{t}_{i}}, \hat{t}_{i})$ 
7:  $\mathbf{c}_{\hat{t}_{i}} \leftarrow -\frac{1+\eta^{2}}{2}g_{\hat{t}_{i}}^{2}\nabla\log\frac{d_{\boldsymbol{\phi}_{\infty}}(\nu_{\tau_{\hat{t}_{i}}}\mathbf{x}_{\hat{t}_{i}}, \tau_{\hat{t}_{i}})}{1-d_{\boldsymbol{\phi}_{\infty}}(\nu_{\tau_{\hat{t}_{i}}}\mathbf{x}_{\hat{t}_{i}}, \tau_{\hat{t}_{i}})}\ (\mathbf{Eq.}\ (9))$ 
8:  $\mathbf{g}_{\hat{t}_{i}} \leftarrow -\frac{1+\eta^{2}}{2}g_{\hat{t}_{i}}^{2}\nabla\log p_{\boldsymbol{\psi}_{\infty}}(y|\mathbf{x}_{\hat{t}_{i}}, \hat{t}_{i})$ 
9:  $\mathbf{x}_{t_{i-1}} \leftarrow \mathbf{x}_{\hat{t}_{i}} + (t_{i-1} - \hat{t}_{i})(\mathbf{s}_{\hat{t}_{i}} + w_{\hat{t}_{i}}^{DG}\mathbf{c}_{\hat{t}_{i}} + w_{\hat{t}_{i}}^{CG}\mathbf{g}_{\hat{t}_{i}})$ 
10:  $\mathbf{x}_{t_{i-1}} \leftarrow \mathbf{x}_{t_{i-1}} + \eta g_{\hat{t}_{i}}\sqrt{t_{i-1} - \hat{t}_{i}}\boldsymbol{\epsilon}'_{i}$ 
11:  $\mathbf{end}\ \mathbf{for}$ 

error  $E_{\theta_{\infty},\phi}$  by imposing an additional axial degree of freedom  $\phi$ . The score error  $E_{\theta_{\infty}}$  is no longer optimizable with  $\mathcal{L}_{\theta}$  of Eq. (3), but the reparametrized error  $E_{\theta_{\infty},\phi}$  could be further optimizable with an alternative loss  $\mathcal{L}_{\phi}$  of Eq. (5), see Figure 4 for a schematic visualization.

## 3.4. Connection with Classifier Guidance

The Classifier Guidance (CG) (Dhariwal & Nichol, 2021) is a milestone technique to guide a sample with a pretrained classifier  $p_{\psi_{\infty}}(c|\mathbf{x}_t,t)$ . The classifier-guided generative process is  $d\mathbf{x}_t = [\mathbf{f}(\mathbf{x}_t,t) - g^2(t)(\mathbf{s}_{\theta_{\infty}}(\mathbf{x}_t,t) + \nabla \log p_{\psi_{\infty}}(y|\mathbf{x}_t,t))] d\bar{t} + g_t d\bar{\mathbf{w}}_t$ . This is equivalent to sampling from the joint distribution of  $(\mathbf{x}_t,y)$  because

$$\nabla \log p_r^t(\mathbf{x}_t, y) = \nabla \log p_r^t(\mathbf{x}_t) + \nabla \log p(y|\mathbf{x}_t, t)$$
$$\approx \mathbf{s}_{\theta_{\infty}}(\mathbf{x}_t, t) + \nabla \log p_{\psi_{\infty}}(y|\mathbf{x}_t, t),$$

where  $p(y|\mathbf{x}_t,t)$  is the oracle classifier at t. The classifier guidance provides auxiliary information on a sample path by evaluating whether the sample is correctly classified by the class label y, or not. In contrast, the discriminator guidance is label-agnostic, and it gives distinctive information on whether the sample path is realistic or unrealistic.

As sampling from the joint distribution of  $(\mathbf{x}_t, y)$  is valid only if the score estimation is accurate, the discriminator guidance would have a synergistic effect with the classifier guidance by adjusting the inaccurate score estimation. We suggest the combination of guidance techniques by

$$d\mathbf{x}_{t} = \left[ \mathbf{f}(\mathbf{x}_{t}, t) - g^{2}(t) \left( (\mathbf{s}_{\boldsymbol{\theta}_{\infty}} + w_{t}^{DG} \mathbf{c}_{\boldsymbol{\phi}_{\infty}}) (\mathbf{x}_{t}, t) + w_{t}^{CG} \nabla \log p_{\boldsymbol{\psi}_{\infty}}(c | \mathbf{x}_{t}, t) \right) \right] d\bar{t} + g(t) d\bar{\mathbf{w}}_{t},$$
(7)

where  $w_t^{DG}$  and  $w_t^{CG}$  are the time-dependent weights, respectively. The two pieces of information could ideally guide the sample toward the common likely region of classifier and discriminator in a complementary way.

Algorithm 2 describes the full details of our sampling procedure for Eq. (7). The algorithm reduces the samplers of DDPM (Ho et al., 2020; Dhariwal & Nichol,

Table 1: Algorithm 2 includes DDPM, DDIM, and EDM samplers.

Sampler	$\gamma_t$	η	$w_t^{CG}$	$w_t^{DG}$
DDPM	0	1	0	0
DDIM	0	0	0	0
EDM	$\geq 0$	0	0	0
ADM-G	0	1	>0	0
EDM-G++	$\geq 0$	0	0	>0
ADM-G++	0	1	>0	>0

2021), DDIM (Song et al., 2020a), and EDM (Karras et al., 2022) with corresponding hyperparameters by Table 1. Our sampler is denoted as the postfix with **G++** upon a basic sampler by a prefix. See Appendix D.1.

## 4. Related Works

A line of research merges diffusion models with GAN models. Zheng et al. (2022b); Lyu et al. (2022) synthesize the diffused data  $\mathbf{x}_{\sigma_{mid}}$  with a GAN generator (by putting  $\mathbf{x}_T$  as generator's input), and denoise  $\mathbf{x}_{\sigma_{mid}}$  to  $\mathbf{x}_0$  with a diffusion model. Xiao et al. (2022) exchange thousands of denoising steps with a small number of sequential conditional GAN generators. Wang et al. (2022) utilize the diffusion concept to train GAN. On the contrary, Jolicoeur-Martineau et al. (2020) train the diffusion model with an adversarial loss. The diffusion model and GAN in previous works, however, do not interplay with each other in generation process after their training. In contrast, the discriminator in DG intervenes in generation process, directly. Another difference to previous research is that we train our discriminator without any generator, so discriminator training is stable.

Among GAN literature, Azadi et al. (2019) best align with our design concept. After the GAN training, Azadi et al. (2019) use the discriminator to estimate the density ratio  $p_r/p_g$ , where  $p_g$  is the sample distribution of the trained generator. Then, Azadi et al. (2019) accept  $\mathbf{x} \sim p_g$  with probability  $\frac{p_r(\mathbf{x})}{Mp_g(\mathbf{x})}$ , where  $M = \sup_{p_g(\mathbf{x})} \frac{p_r(\mathbf{x})}{p_g(\mathbf{x})}$ . Hence, Azadi et al. (2019) aim at sampling from  $p_r$  by rejection. Contrast to GAN generation, diffusion models are reletively slow for sample generation, and the rejection sampler is hardly applicable in practice. DG maximizes  $\frac{p_r^t}{p_\theta^t}$  in the same spirit of gradient descent, and it could be approximately viewed as an *importance sampler* with an importance weight  $\frac{p_r^t}{p_\theta^t}$  and a sample distribution  $p_\theta^t$ . Thus, DG does not require sample rejection, and it is scalable to high-dimensions.

#### 5. Experiments

## 5.1. A Toy 2-dimensional Case

Figure 5 shows the experimental result of a tractable 2-dimensional toy case. We train a 4-layered MLP discriminator with 256 neurons until convergence, and we hypothesize

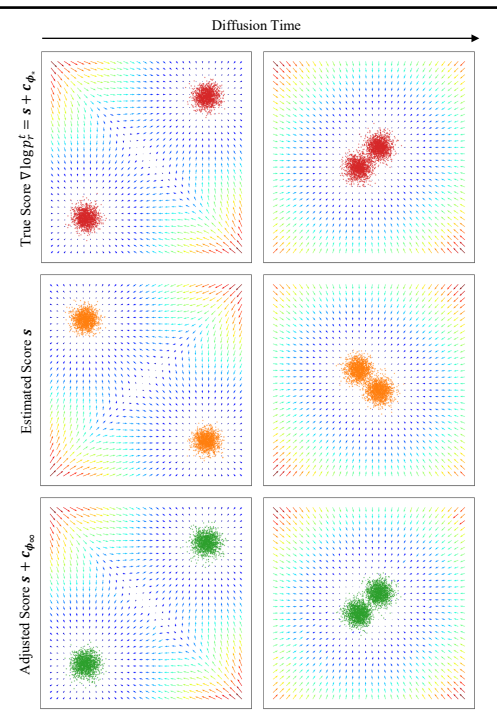


Figure 5: Comparison of the true data score, estimated score, and adjusted score with their samples in a toy 2-dimensional case. We assume  $p_r(\mathbf{x}) := \frac{1}{2}\mathcal{N}(\mathbf{x}; (10,10)^T, \mathbf{I}) + \frac{1}{2}\mathcal{N}(\mathbf{x}; (-10,-10)^T, \mathbf{I})$  as data distribution and  $p_g(\mathbf{x}) := \frac{1}{2}\mathcal{N}(\mathbf{x}; (10,-10)^T, \mathbf{I}) + \frac{1}{2}\mathcal{N}(\mathbf{x}; (-10,10)^T, \mathbf{I})$  as generative distribution with an incorrect score  $\mathbf{s}(\mathbf{x}_t,t) := \nabla \log p_g^t(\mathbf{x}_t)$ . We solve the probability-flow ODE (Song et al., 2020b) to visualize samples from each score function.

an incorrect score function  $\mathbf{s} := \nabla \log p_g^t$  (for a synthetic generative distribution  $p_g$ ) that misfits to the data score. If there is no guidance, the incorrect score  $\mathbf{s}$  will generate samples from a wrong distribution as in the middle row of Figure 5. On the contrary,  $\mathbf{s} + \mathbf{c}_{\phi_{\infty}}$  successfully guides  $\mathbf{s}$  to  $\nabla \log p_r^t$ , see Figures 14 and 15 for additional visualization.

#### 5.2. Image Generation

We experiment on CIFAR-10, CelebA/FFHQ 64x64, and ImageNet 256x256. We use the pre-trained networks on CIFAR-10 and FFHQ from Karras et al. (2022); Vahdat et al. (2021), CelebA from Kim et al. (2022b) and ImageNet from Dhariwal & Nichol (2021); but we emphasize that our method could be universally applicable regardless of the choice of a diffusion model and its implementation.

**Discriminator Network.** We use the encoder of U-Net structure<sup>1</sup> as our discriminator network. For pixel-diffusion models, we attach two time-embedded U-Net encoders: the pre-trained ADM classifier (Dhariwal & Nichol, 2021) and an auxiliary (shallow) U-Net encoder. We put  $(\mathbf{x}_t, t)$  to the

<sup>&</sup>lt;sup>1</sup>We tested MLP, ResNet18, and a transformer, but the U-Net performed the best for DG.

Table 2: Performance on CIFAR-10.

	Diffusion Space	NFE↓	Uncondi NLL↓	tional FID↓	Conditional FID↓
VDM (Kingma et al., 2021)	Data	1000	2.49	7.41	-
DDPM (Ho et al., 2020)	Data	1000	3.75	3.17	-
iDDPM (Nichol & Dhariwal, 2021)	Data	1000	3.37	2.90	-
STDDPM (Kim et al., 2022b)	Data	2000	2.91	2.47	-
INDM (Kim et al., 2022a)	Latent	2000	3.09	2.28	-
CLD-SGM (Dockhorn et al., 2022)	Data	312	3.31	2.25	-
NCSN++ (Song et al., 2020b)	Data	2000	3.45	2.20	-
LSGM (Vahdat et al., 2021)	Latent	138	3.43	2.10	-
NCSN++-G (Chao et al., 2022)	Data	2000	-	-	2.25
EDM <sup>†</sup> (random seed)	Data	39	2.60	2.03	1.82
EDM (reported, manual seed)	Data	35	2.60	1.97	1.79
		120			
LSGM-G++	Latent	138	3.42	1.94	
EDM-G++	Data	35	<u>2.55</u>	1.77	1.64

<sup>&</sup>lt;sup>†</sup> We recalculate FID of EDM (Karras et al., 2022) under a random seed for a fair comparison with previous research. We report our performances under the random seed by default.

Table 3: FID comparison on CelebA and FFHQ.

	NFE↓	CelebA	FFHQ
DDPM++ (Song et al., 2020b)	131	2.32	-
STDDPM (Kim et al., 2022b)	131	1.90	-
Soft Diffusion (Daras et al., 2022)	300	1.85	-
INDM (Kim et al., 2022a)	132	1.75	-
Diffusion StyleGAN2 (Wang et al., 2022)	1	1.69	-
EDM (Karras et al., 2022)	79	-	2.39
STDDPM-G++	131	1.34	-
EDM-G++	<u>71</u>	-	1.98

ADM classifier, and we extract the latent  $\mathbf{z}_t$  of  $\mathbf{x}_t$  from the last pooling layer of the pre-trained classifier. Then, we put  $(\mathbf{z}_t,t)$  to the auxiliary U-Net encoder and predict real/fake by its output. We freeze the ADM classifier, and we only fine-tune the U-Net encoder as default. Not to mention that fine-tuning save the training cost, fine-tuning performs better or equivalent to training the entire architecture (Kato & Teshima, 2021). For latent-diffusion models, we train the U-Net encoder from scratch. We train a class-conditional discriminator for the class-conditional generation. See Table 8 for detailed training configuration.

**Quantitative Analysis.** We achieve new SOTA FIDs on all datasets including CIFAR-10, CelebA, FFHQ, and ImageNet. On CIFAR-10, Table 2 shows that DG is effective in both pixel-diffusion (EDM) and latent-diffusion (LSGM) models. Other than DG, we use all the hyperparameters of EDM and LSGM, so the performance gain purely comes from DG. Besides, the result empirically shows that DG works with samplers of small NFEs. The gain of DG is also notable on human-face datasets in Table 3.

On ImageNet (Table 4), when IS and precision of a model reach the level of the validation dataset (232.21 for IS and 0.75 for precision), optimizing other metrics such as FID, sFID, and recall become more important. However, there is a trade-off between FID and recall, so we report three experimental results. In the recall-best setting of ADM-G++ (cfg=0.10), our model is comparable with LDM-4 and ADM (w/o CG) in terms of recall, but significantly outperforms the baselines in FID and IS. On top of that, our recall-best result beats ADM-G in FID. Figure 2-(c) shows the samples from the recall-best setting, which is as diverse as ADM and

Table 4: Performance on ImageNet 256x256.

Model	CG	DG	EDS	$\text{FID}{\downarrow}$	$\text{sFID}{\downarrow}$	IS↑	Prec↑	Rec↑	F1↑
Validation Data	-	-	-	1.68	3.67	232.21	0.75	0.66	0.70
LDM-4 (Rombach et al., 2022) ADM (Dhariwal & Nichol, 2021) ADM-G++ (cfg=0.10)	X X V	X X V	X X	10.56 10.94 <b>4.45</b>	6.02 5.38	103.49 100.98 190.71	0.71 0.69 <b>0.76</b>	0.62 0.63 0.60	0.66 0.66 <b>0.67</b>
LDM-4-G (cfg=1.25) LDM-4-G (cfg=1.50) ADM-G (cfg=1.50) ADM-G (cfg=0.75) ADM-G++ (cfg=0.25)	1111	× × × ×	× × × ✓	3.95 3.60 4.59 4.01 3.73	5.25 5.15 5.03	178.22 <b>247.67</b> 186.70 217.25 204.49	0.81 0.87 0.82 0.82 0.78	0.55 0.48 0.52 0.53 <b>0.59</b>	0.66 0.62 0.64 0.64 <b>0.67</b>
ADM-G++ (cfg=0.75)	1	1	1	3.18	4.53	255.74	0.84	0.53	0.65







(a) Original Data

(b) EDM

(c) EDM-G++

Figure 6: Comparison of (a) original sample, and the average of 100 regenerated samples of (b) EDM and (c) EDM-G++ on FFHQ. The regeneration FID is 1.25 (w/o DG) and 1.09 (w/ DG) if we perturb data by the standard Gaussian.

as precise as ADM-G. In the FID-best setting of ADM-G++ (cfg=0.75), we achieve SOTA in FID and sFID with strictly better IS/precision than both reference validation and ADM-G (cfg=0.75) (Zheng et al., 2022a). See Table 8 for detailed hyperparameters and Appendix D.3 for uncurated samples.

Qualitative Analysis. Figure 6 compares the original sample to the averages of its regenerated 100 samples (Meng et al., 2021) on FFHQ. For the regeneration, we perturb the original sample of Figure 6-(a) with a random noise from the standard Gaussian, and solve the probability flow ODE. We choose a small tolerance for the ODE solver, so the discrepancy purely originates from the score accuracy. Ideally, as the sampler is deterministic, we expect perfect regeneration if the score estimation is accurate. The poor regeneration of Figure 6-(b) is a diagnostic of the mismatch between the forward (Eq. 1) and generative (Eq. 4) SDEs. In contrast, Figure 6-(c) demonstrates the coincidence of the forward (Eq. 1) and adjusted generative (Eq. 6) SDEs.

Figure 7 shows that the trained discriminator is able to accurately distinguish between diffusion paths from real data and sample data. By utilizing the adjusted score, the generated sample path deceives the discriminator, resulting in the density-ratio curve of the adjusted generative SDE (Eq. 6) closely approximating that of the data forward SDE.

Figure 8 illustrates the effect of DG by sampling NFEs on CIFAR-10. As NFE decreases, the discretization error dominates the sampling error (De Bortoli, 2022), and the gain from DG becomes suboptimal. We leave it as a future work to fit DG on samplers with extremely small NFEs. See Appendix D.2 for more ablation studies.

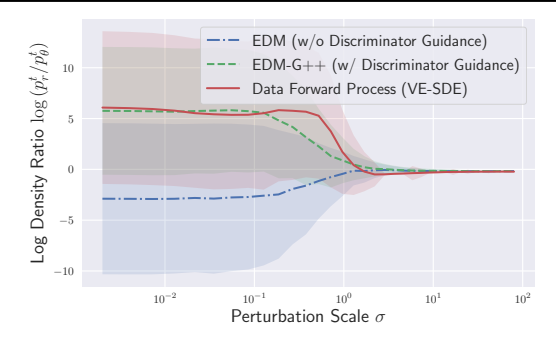


Figure 7: Comparison of sample trajectories with respect to the density-ratio on FFHQ.

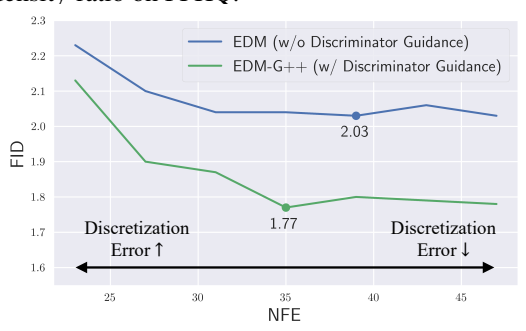


Figure 8: Ablation study for NFE on CIFAR-10.

Figure 9 illustrates the negative log-probability  $-\log \mathcal{N}(F(\mathbf{x}); \boldsymbol{\mu}_{data}, \boldsymbol{\Sigma}_{data})$  on ImageNet 256, where  $F(\mathbf{x})$  is the feature map² of sFID (Nash et al., 2021) that is specialized in capturing the spatial features. Figure 9 compares 50k-samples from ADM-G, ADM-G++, and the validation data, and it shows that the feature distribution of ADM-G++ aligns with the validation data in the heavy-tail. Given the tail of the negative log-probability represents for diverse but rare data, Figure 9 demonstrates that ADM-G++ generates not only frequently seen data but rarely observed data in training. Constrast to ADM-G++, the diversity of ADM-G is limited, see Figure 23 for detailed analysis.

## 5.3. Image-2-Image Translation

The discriminator guidance could be applied to the Image-2-Image (I2I) translation task. I2I (Meng et al., 2021) denoise a perturbed source image with a score network trained on the target domain. For discriminator training, we first translate source training images, and then we aggregate these translated images with source images to a fake dataset  $\mathcal{G}$ . By specifying  $\mathcal{D}$  as target images, we follow Algorithm 1 to train the discriminator. DG avoids going neither the *source* domain nor the *translated* domain, and it leads to the *target* domain in Figure 10-(a). Empirically, the curve in Figure 10-(b) shows that the discriminator guidance remedies the trade-off between *realism* (to target) and *faithfulness* (with source). We leave Appendix C for details.

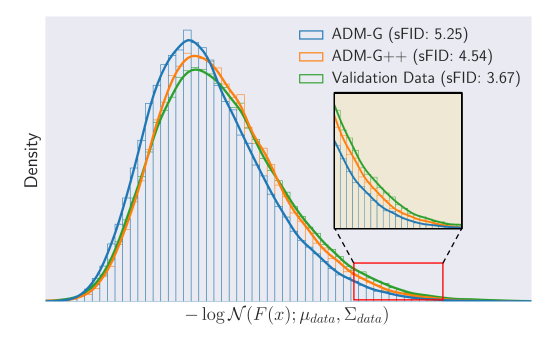


Figure 9: ADM-G++ is as diverse as the validation data.

## 6. Discussion

This section discusses two potential directions for the future development of DG. Table 5 proposes that DG

Table 5: Discriminator guidance is a new paradigm of estimating the data score with a different estimation target and a different training loss.

Model	Estimation Target	Training Loss
Score-based	Data Score	f-Divergence
DG (Ours)	Density-Ratio	Bregman Divergence

could be a new framework alternative to the common practice of diffusion models in terms of the estimation target function and the training loss function. First, regarding the estimation target, the whole methodology in Section 3 could also be applied for any score network, regardless of its estimation accuracy. That is, the data score is the summation of a score estimation (with arbitrary precision) and its corresponding correction term organized by a density-ratio (Theorem 1), and DG estimates the density-ratio instead of training the score network. However, the popular target function of diffusion models is either data score ( $\|\mathbf{s}_{\theta} - \nabla \log p_r^t\|$   $\downarrow$ ) (Song et al., 2020b) , noise ( $\|\epsilon_{\theta} - \epsilon\|$   $\downarrow$ ) (Ho et al., 2020), or data ( $\|\hat{\mathbf{x}}_{\theta} - \mathbf{x}\|$   $\downarrow$ ) (Kingma et al., 2021), which are essentially identical to train the score network.

In theory, the density-ratio framework guarantees to estimate the data distribution  $p_{\theta,\phi_*}$  for any score  $\mathbf{s}_{\theta}$  with arbitrary precision, at its corresponding optimal point  $\phi_*$ . To see whether this theory indeed holds in practice, we consider the inaccurate scores  $\mathbf{s}_{\theta_n}$  as testbeds, where n is the  $\theta$ -training epoch. Figure 11 illustrates that the density-ratio training framework is suboptimal to the score training framework for all n.

In order to gain an insight regarding the suboptimal accuracy, we conduct an ablation study in Table 6 to investigate the estimation accuracy in terms of the diffusion scale. The case of (S) replaces the score function only on the range of small scales  $[0,\sigma_{mid}]$ , and (L) substitutes the score function on  $[0,\sigma_{mid}]$ . We observe two implications from Table 6: from (S),  $\mathbf{s}_{\theta_{25}} + \mathbf{c}_{\phi_{\infty}}$  deviates from the data score on small scales; from (L),  $\mathbf{s}_{\theta_{25}} + \mathbf{c}_{\phi_{\infty}}$  is as accurate as  $\mathbf{s}_{\theta_{\infty}}$  on large scales. In addition, Figure 12 additionally ablates to investigate the impact of our framework under detailed scale

<sup>&</sup>lt;sup>2</sup>of the first 7 channels from the intermediate mixed\_6/conv of the inception network (Szegedy et al., 2016).



(a) SDEdit+DG improves translation quality

(b) Realism vs. Faithfulness

Figure 10: I2I translation task. (a) The discriminator-guided translated samples from SDEdit are more realistic than non-guided samples from SDEdit given the same translation starting time  $t_{mid} = 0.5$ . (b) DG partially mitigates the trade-off between realism and faithfulness. Also, the weighted DG improves sample realism without hurting faithfulness.

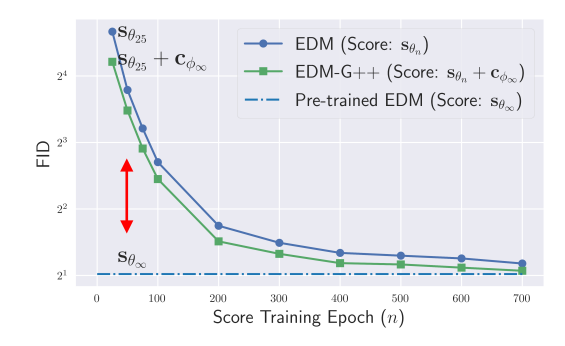


Figure 11: FID by score network training on CIFAR-10. Table 6: The adjusted score  $\mathbf{s}_{\theta_{25},\phi_{\infty}}$  could be a substitute of  $\mathbf{s}_{\theta_{\infty}}$  in the large-time on CIFAR-10.

Cases	$[0, \sigma_{mid}]$	]	$[\sigma_{mid}, \sigma_{m}]$	$\sigma_{mid}$	FID	
	$\mathbf{s}_{\boldsymbol{\theta}_{25}} + \mathbf{c}_{\boldsymbol{\phi} \infty}$	$\mathbf{s}_{oldsymbol{ heta}_{\infty}}$	$\mathbf{s}_{\boldsymbol{\theta}_{25}} + \mathbf{c}_{\boldsymbol{\phi} \infty}$	$\mathbf{s}_{oldsymbol{ heta}_{\infty}}$		
(S)	✓	1	<i>,</i>		10	19.20 1.95
(L)		✓ ✓	<b>✓</b>	/	10	1.95 2.03

change. Figure 12 indicates that the accuracy of  $\mathbf{s}_{\theta_{25}} + \mathbf{c}_{\phi_{\infty}}$  rapidly deteriorates as  $\sigma_{mid}$  drops less than 10, assuring the implication of Table 6 that the density-ratio framework may be a suitable replacement for the previous score training framework on large diffusion scales.

The second direction of DG development in Table 5 is about its loss function. The training loss of the density-ratio could be generalized as the h-Bregman divergence (Sugiyama et al., 2012), which is a class of statistical divergences (Amari, 2009) distinctive to the f-divergence (Nowozin et al., 2016). In the time-dependent case with the target density-ratio  $r_*^t = \frac{p_r^t}{p_{\theta_\infty}^t}$  and its neural estimation  $r_\phi^t = \frac{d_\phi}{1-d_\phi}$ , we define the h-Bregman divergence as

$$D_h(r_*^{\cdot}||r_{\phi}^{\cdot}) = \int \lambda(t) \mathbb{E}_{p_{\theta_{\infty}}^t(\mathbf{x}_t)} \left[ h(r_*^t(\mathbf{x}_t)) - h(r_{\phi}^t(\mathbf{x}_t)) - \partial h(r_{\phi}^t(\mathbf{x}_t)) (r_*^t(\mathbf{x}_t) - r_{\phi}^t(\mathbf{x}_t)) \right] d\mathbf{x}_t dt.$$

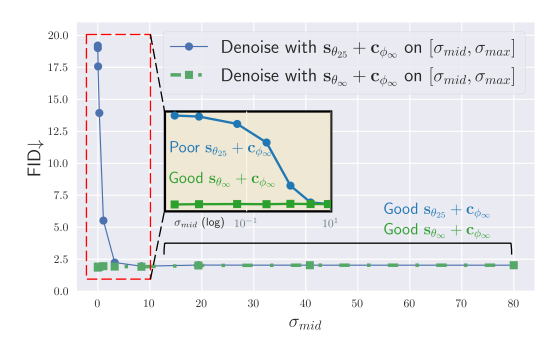


Figure 12: Density-ratio estimation performs as well as score matching framework only on large diffusion scale.

Table 7: Effect of Discriminator Loss on CIFAR-10.

Model	Discriminator Loss	h(r)	FID
EDM			2.03
EDM-G++	UKL (Nguyen et al., 2010) LSIF (Kanamori et al., 2009) BCE ( $\mathcal{L}_{m{\phi}}$ of Eq. (5))	$r \log r - r  (r-1)^2/2  r \log r - (1+r) \log (1+r)$	1.84 1.84 1.77

Both of the previous models and DG optimize their target loss with non-overlaping divergence families: f-divergence for diffusion models (Song et al., 2021; Kim et al., 2022b) and h-Bregman divergence for the discriminator guidance<sup>3</sup>. Empirically, Table 7 demonstrates that DG works for various h functions, and we set BCE  $\mathcal{L}_{\phi}$  of Eq. (5) as default because BCE performs the best out of representative h-Bregman divergences. We leave it as a future work to find a better h-function for DG.

#### 7. Conclusion

This paper refines the denoising process with an adjusted score estimation. With the proposed method, we could further optimize the divergence of a pre-trained score model. Empirical results demonstrate that our approach achieves new SOTA FIDs on all datasets. The deepfake images are one of the potential risks of the negative usage of this work.

 $<sup>^{3}</sup>$ BCE of Eq. (5) is the unique divergence that belongs both f-divergence and h-Bregman divergence (Amari, 2009).

#### References

- Amari, S.-I. *alpha*-divergence is unique, belonging to both *f*-divergence and bregman divergence classes. *IEEE Transactions on Information Theory*, 55(11):4925–4931, 2009.
- Ascher, U. M. and Petzold, L. R. Computer methods for ordinary differential equations and differential-algebraic equations, volume 61. Siam, 1998.
- Azadi, S., Olsson, C., Darrell, T., Goodfellow, I., and Odena, A. Discriminator rejection sampling. In *International Conference on Learning Representations*, 2019.
- Chao, C.-H., Sun, W.-F., Cheng, B.-W., Lo, Y.-C., Chang, C.-C., Liu, Y.-L., Chang, Y.-L., Chen, C.-P., and Lee, C.-Y. Denoising likelihood score matching for conditional score-based data generation. In *International Conference* on Learning Representations, 2022.
- Daras, G., Delbracio, M., Talebi, H., Dimakis, A. G., and Milanfar, P. Soft diffusion: Score matching for general corruptions. *arXiv* preprint arXiv:2209.05442, 2022.
- De Bortoli, V. Convergence of denoising diffusion models under the manifold hypothesis. *arXiv preprint arXiv:2208.05314*, 2022.
- Dhariwal, P. and Nichol, A. Diffusion models beat gans on image synthesis. *Advances in Neural Information Processing Systems*, 34, 2021.
- Dockhorn, T., Vahdat, A., and Kreis, K. Score-based generative modeling with critically-damped langevin diffusion. In *International Conference on Learning Representations*, 2022.
- Dormand, J. R. and Prince, P. J. A family of embedded runge-kutta formulae. *Journal of computational and applied mathematics*, 6(1):19–26, 1980.
- Hastie, T., Tibshirani, R., Friedman, J. H., and Friedman, J. H. *The elements of statistical learning: data mining, inference, and prediction*, volume 2. Springer, 2009.
- Ho, J., Jain, A., and Abbeel, P. Denoising diffusion probabilistic models. *Advances in Neural Information Processing Systems*, 33:6840–6851, 2020.
- Ho, J., Saharia, C., Chan, W., Fleet, D. J., Norouzi, M., and Salimans, T. Cascaded diffusion models for high fidelity image generation. arXiv preprint arXiv:2106.15282, 2021.
- Ho, J., Salimans, T., Gritsenko, A., Chan, W., Norouzi, M., and Fleet, D. J. Video diffusion models. arXiv preprint arXiv:2204.03458, 2022.

- Jolicoeur-Martineau, A., Piché-Taillefer, R., Combes, R. T. d., and Mitliagkas, I. Adversarial score matching and improved sampling for image generation. arXiv preprint arXiv:2009.05475, 2020.
- Kanamori, T., Hido, S., and Sugiyama, M. A least-squares approach to direct importance estimation. *The Journal of Machine Learning Research*, 10:1391–1445, 2009.
- Karras, T., Aittala, M., Aila, T., and Laine, S. Elucidating the design space of diffusion-based generative models. *arXiv* preprint arXiv:2206.00364, 2022.
- Kato, M. and Teshima, T. Non-negative bregman divergence minimization for deep direct density ratio estimation. In *International Conference on Machine Learning*, pp. 5320– 5333. PMLR, 2021.
- Kawar, B., Elad, M., Ermon, S., and Song, J. Denoising diffusion restoration models. arXiv preprint arXiv:2201.11793, 2022.
- Kim, D., Na, B., Kwon, S. J., Lee, D., Kang, W., and Moon, I.-C. Maximum likelihood training of implicit nonlinear diffusion models. *arXiv preprint arXiv:2205.13699*, 2022a.
- Kim, D., Shin, S., Song, K., Kang, W., and Moon, I.-C. Soft truncation: A universal training technique of score-based diffusion model for high precision score estimation. In *International Conference on Machine Learning*, pp. 11201–11228. PMLR, 2022b.
- Kim, Y., Kim, D., Lee, H., and Moon, I.-c. Unsupervised controllable generation with score-based diffusion models: Disentangled latent code guidance. In *NeurIPS 2022 Workshop on Score-Based Methods*.
- Kingma, D. P., Salimans, T., Poole, B., and Ho, J. Variational diffusion models. In *Advances in Neural Information Processing Systems*, 2021.
- Lyu, Z., Xu, X., Yang, C., Lin, D., and Dai, B. Accelerating diffusion models via early stop of the diffusion process. *arXiv* preprint arXiv:2205.12524, 2022.
- Meng, C., He, Y., Song, Y., Song, J., Wu, J., Zhu, J.-Y., and Ermon, S. Sdedit: Guided image synthesis and editing with stochastic differential equations. *arXiv* preprint *arXiv*:2108.01073, 2021.
- Nash, C., Menick, J., Dieleman, S., and Battaglia, P. Generating images with sparse representations. In *International Conference on Machine Learning*, pp. 7958–7968. PMLR, 2021.
- Nguyen, X., Wainwright, M. J., and Jordan, M. I. Estimating divergence functionals and the likelihood ratio by convex

- risk minimization. *IEEE Transactions on Information Theory*, 56(11):5847–5861, 2010.
- Nichol, A. and Dhariwal, P. Improved denoising diffusion probabilistic models. *arXiv preprint arXiv:2102.09672*, 2021.
- Nowozin, S., Cseke, B., and Tomioka, R. f-gan: Training generative neural samplers using variational divergence minimization. *arXiv preprint arXiv:1606.00709*, 2016.
- Ramesh, A., Dhariwal, P., Nichol, A., Chu, C., and Chen, M. Hierarchical text-conditional image generation with clip latents. *arXiv preprint arXiv:2204.06125*, 2022.
- Rhodes, B., Xu, K., and Gutmann, M. U. Telescoping density-ratio estimation. *Advances in neural information processing systems*, 33:4905–4916, 2020.
- Rombach, R., Blattmann, A., Lorenz, D., Esser, P., and Ommer, B. High-resolution image synthesis with latent diffusion models. In *Proceedings of the IEEE/CVF Conference on Computer Vision and Pattern Recognition*, pp. 10684–10695, 2022.
- Russakovsky, O., Deng, J., Su, H., Krause, J., Satheesh, S., Ma, S., Huang, Z., Karpathy, A., Khosla, A., Bernstein, M., et al. Imagenet large scale visual recognition challenge. *International journal of computer vision*, 115(3): 211–252, 2015.
- Saharia, C., Chan, W., Saxena, S., Li, L., Whang, J., Denton, E., Ghasemipour, S. K. S., Ayan, B. K., Mahdavi, S. S., Lopes, R. G., et al. Photorealistic text-to-image diffusion models with deep language understanding. arXiv preprint arXiv:2205.11487, 2022.
- Särkkä, S. and Solin, A. *Applied stochastic differential equations*, volume 10. Cambridge University Press, 2019.
- Singer, U., Polyak, A., Hayes, T., Yin, X., An, J., Zhang, S., Hu, Q., Yang, H., Ashual, O., Gafni, O., et al. Make-avideo: Text-to-video generation without text-video data. arXiv preprint arXiv:2209.14792, 2022.
- Song, J., Meng, C., and Ermon, S. Denoising diffusion implicit models. In *International Conference on Learning Representations*, 2020a.
- Song, Y., Sohl-Dickstein, J., Kingma, D. P., Kumar, A., Ermon, S., and Poole, B. Score-based generative modeling through stochastic differential equations. In *International Conference on Learning Representations*, 2020b.
- Song, Y., Durkan, C., Murray, I., and Ermon, S. Maximum likelihood training of score-based diffusion models. *Advances in Neural Information Processing Systems*, 34, 2021.

- Su, X., Song, J., Meng, C., and Ermon, S. Dual diffusion implicit bridges for image-to-image translation. *arXiv* preprint arXiv:2203.08382, 2022.
- Sugiyama, M., Suzuki, T., and Kanamori, T. Density-ratio matching under the bregman divergence: a unified framework of density-ratio estimation. *Annals of the Institute of Statistical Mathematics*, 64(5):1009–1044, 2012.
- Szegedy, C., Vanhoucke, V., Ioffe, S., Shlens, J., and Wojna, Z. Rethinking the inception architecture for computer vision. In *Proceedings of the IEEE conference on computer vision and pattern recognition*, pp. 2818–2826, 2016.
- Vahdat, A., Kreis, K., and Kautz, J. Score-based generative modeling in latent space. *Advances in Neural Information Processing Systems*, 34, 2021.
- Voleti, V., Jolicoeur-Martineau, A., and Pal, C. Mcvd: Masked conditional video diffusion for prediction, generation, and interpolation. *arXiv preprint arXiv:2205.09853*, 5(4.1):4, 2022.
- Wang, Z., Zheng, H., He, P., Chen, W., and Zhou, M. Diffusion-gan: Training gans with diffusion. *arXiv* preprint arXiv:2206.02262, 2022.
- Xiao, Z., Kreis, K., and Vahdat, A. Tackling the generative learning trilemma with denoising diffusion gans. In *International Conference on Learning Representations*, 2022.
- Zheng, G., Li, S., Wang, H., Yao, T., Chen, Y., Ding, S., and Li, X. Entropy-driven sampling and training scheme for conditional diffusion generation. In *European Conference on Computer Vision*, pp. 754–769. Springer, 2022a.
- Zheng, H., He, P., Chen, W., and Zhou, M. Truncated diffusion probabilistic models and diffusion-based adversarial auto-encoders. *arXiv* preprint arXiv:2202.09671, 2022b.

## A. Proofs and More Analysis

### A.1. Proof of Theorem 1

Throughout the section, we assume that the assumptions made in Appendix A of Song et al. (2021) hold.

**Theorem 1.** Suppose  $p_{\theta}$  be the solution of the time-reversal generative process of Eq. (4). Let  $p_{\tau}^{t}$  and  $p_{\theta}^{t}$  be the marginal densities (at t) of the forward-time SDE  $d\mathbf{x}_{t} = \mathbf{f}(\mathbf{x}_{t}, t) dt + g(t) d\mathbf{w}_{t}$  starting from  $p_{\tau}$  and  $p_{\theta}$ , respectively. If  $\mathbf{s}_{\theta}(\mathbf{x}, T) = \nabla \log \pi(\mathbf{x})$ , where  $\pi$  is the prior distribution, and the log-likelihood  $\log p_{\theta}$  equals its evidence lower bound  $\mathcal{L}_{\theta}$ , then

$$d\mathbf{x}_t = \left[ \mathbf{f}(\mathbf{x}_t, t) - g^2(t) \nabla \log p_r^t(\mathbf{x}_t) \right] d\bar{t} + g(t) d\bar{\mathbf{w}}_t,$$

coincides with a diffusion process with adjusted score,

$$d\mathbf{x}_t = \left[ \mathbf{f}(\mathbf{x}_t, t) - q^2(t)(\mathbf{s}_{\theta} + \mathbf{c}_{\theta})(\mathbf{x}_t, t) \right] d\bar{t} + q(t) d\bar{\mathbf{w}}_t,$$

for 
$$\mathbf{c}_{\theta}(\mathbf{x}_t, t) := \nabla \log \frac{p_r^t(\mathbf{x}_t)}{p_{\theta}^t(\mathbf{x}_t)}$$
.

To prove the theorems, we define a family of rotation-free score functions by  $S_{sol}$  in Definition 1.

**Definition 1** (Definition 1 of Kim et al. (2022a)). Let  $\mathbf{S}_{div} = \{\mathbf{v} : \mathbb{R}^d \to \mathbb{R}^d | \mathbf{v} = \nabla \log p \text{ for some probability } p\}$  be the family of rotation-free score functions. Define  $\mathbf{S}_{sol}$  be a family of time-conditioned score network s that satisfies the following: there exists  $q_0$  and  $q_t$  such that  $\mathbf{s}(\mathbf{x},t) = \nabla \log q_t(\mathbf{x})$  almost everywhere, where  $q_t$  is the marginal density at time t of  $d\mathbf{x}_t = \mathbf{f}(\mathbf{x}_t,t) dt + g(t) d\mathbf{w}_t$ , starting from  $\mathbf{x}_0 \sim q_0$ .

With Definition 1, Kim et al. (2022a) introduces the necessary and sufficient condition for  $\mathbf{s}_{\theta} \in \mathbf{S}_{sol}$ .

**Lemma 1** (Theorem 2 of Kim et al. (2022a)). Suppose  $s_{\theta}$  is twice continuously differentiable with respect to x. Then,

$$D_{KL}(p_r \| p_{\boldsymbol{\theta}}) = \frac{1}{2} \int_0^T g^2(t) \mathbb{E} \left[ \| \mathbf{s}_{\boldsymbol{\theta}}(\mathbf{x}_t, t) - \nabla \log p_r^t(\mathbf{x}_t) \|_2^2 \right] dt + D_{KL}(p_r^T \| \pi)$$

holds if and only if  $\mathbf{s}_{\theta} \in \mathbf{S}_{sol}$ .

Lemma 2. The log-likelihood equals the evidence lower bound if and only if

$$D_{KL}(p_r \| p_{\boldsymbol{\theta}}) = \frac{1}{2} \int_0^T g^2(t) \mathbb{E} \left[ \| \mathbf{s}_{\boldsymbol{\theta}}(\mathbf{x}_t, t) - \nabla \log p_r^t(\mathbf{x}_t) \|_2^2 \right] dt + D_{KL}(p_r^T \| \pi).$$

Combining Lemmas 1 and 2, we yield that  $s_{\theta} \in S_{sol}$  if and only if the log-likelihood equals the evidence lower bound. Now, we provide the proof.

Proof of Theorem 1. From Lemmas 1 and 2 combined, we obtain  $\mathbf{s}_{\theta} \in \mathbf{S}_{sol}$ . Therefore, there exists  $q_0$  such that  $q_t$  is the marginal density of  $d\mathbf{x}_t = \mathbf{f}(\mathbf{x}_t, t) dt + g(t) d\mathbf{w}_t$  and satisfies  $\mathbf{s}_{\theta}(\mathbf{x}_t, t) = \nabla \log q_t(\mathbf{x}_t)$  almost everywhere. Then, the solution of the generative process

$$d\mathbf{x}_{t} = \left[\mathbf{f}(\mathbf{x}_{t}, t) - g^{2}(t)\mathbf{s}_{\boldsymbol{\theta}}(\mathbf{x}_{t}, t)\right] d\bar{t} + g(t) d\bar{\mathbf{w}}_{t}$$

$$= \left[\mathbf{f}(\mathbf{x}_{t}, t) - g^{2}(t)\nabla \log q_{t}(\mathbf{x}_{t})\right] d\bar{t} + g(t) d\bar{\mathbf{w}}_{t},$$
(8)

starting from  $q_T$  at T attains  $q_t$  as its marginal density at t. As  $\mathbf{s}_{\theta}(\mathbf{x}_T, T) = \nabla \log \pi(\mathbf{x}_T)$ , the marginal density  $q_T$  at T becomes the prior distribution  $\pi$ , and we get  $q_0 = p_{\theta}$ .

Hence,  $p_{\theta}^t$  is the marginal density of  $d\mathbf{x}_t = \mathbf{f}(\mathbf{x}_t, t) dt + g(t) d\mathbf{w}_t$ , starting from  $\mathbf{x}_0 \sim p_{\theta} = q_0$ . From the uniqueness, we conclude that  $p_{\theta}^t = q_t$  for all t and thus  $\mathbf{s}_{\theta}(\mathbf{x}_t, t) = \nabla \log p_{\theta}^t(\mathbf{x}_t)$ , which leads the desired result.

#### A.2. Proof of Theorem 2

**Theorem 2.** If the assumptions of Theorem 1 hold, then

$$D_{KL}(p_r || p_{\boldsymbol{\theta}}) = D_{KL}(p_r^T || \pi) + E_{\boldsymbol{\theta}},$$

$$D_{KL}(p_r || p_{\boldsymbol{\theta}, \boldsymbol{\phi}}) \le D_{KL}(p_r^T || \pi) + E_{\boldsymbol{\theta}, \boldsymbol{\phi}}$$

where

$$E_{\boldsymbol{\theta}} = \frac{1}{2} \int_0^T g^2(t) \mathbb{E}_{p_r^t} \left[ \|\nabla \log p_r^t - \nabla \log p_{\boldsymbol{\theta}}^t \|_2^2 \right],$$

$$E_{\boldsymbol{\theta}, \boldsymbol{\phi}} = \frac{1}{2} \int_0^T g^2(t) \mathbb{E}_{p_r^t} \left[ \|\mathbf{c}_{\boldsymbol{\theta}} - \mathbf{c}_{\boldsymbol{\phi}}\|_2^2 \right] dt.$$

Proof of Theorem 2. We have

$$\begin{split} \mathrm{d}\mathbf{x}_t &= \left[\mathbf{f}(\mathbf{x}_t,t) - g^2(t)(\mathbf{s}_{\theta} + \mathbf{c}_{\phi})\right] \mathrm{d}\bar{t} + g(t) \, \mathrm{d}\bar{\mathbf{w}}_t \\ &= \left[\mathbf{f}(\mathbf{x}_t,t) - g^2(t) \left(\mathbf{s}_{\theta} + \nabla \log \frac{d_{\phi}}{1 - d_{\phi}}\right)\right] \mathrm{d}\bar{t} + g(t) \, \mathrm{d}\bar{\mathbf{w}}_t \\ &= \left[\mathbf{f}(\mathbf{x}_t,t) - g^2(t) \left(\nabla \log p_g^t + \nabla \log \frac{d_{\phi}}{1 - d_{\phi}}\right)\right] \mathrm{d}\bar{t} + g(t) \, \mathrm{d}\bar{\mathbf{w}}_t \\ &= \left[\mathbf{f}(\mathbf{x}_t,t) - g^2(t) \left(\nabla \log p_g^t + \nabla \log \frac{d_{\phi_*}}{1 - d_{\phi_*}} - \nabla \log \frac{d_{\phi_*}}{1 - d_{\phi_*}} + \nabla \log \frac{d_{\phi}}{1 - d_{\phi}}\right)\right] \mathrm{d}\bar{t} + g(t) \, \mathrm{d}\bar{\mathbf{w}}_t \\ &= \left[\mathbf{f}(\mathbf{x}_t,t) - g^2(t) \left(\nabla \log p_g^t + \nabla \log \frac{p_r^t}{p_g^t} - \nabla \log \frac{d_{\phi_*}}{1 - d_{\phi_*}} + \nabla \log \frac{d_{\phi}}{1 - d_{\phi}}\right)\right] \mathrm{d}\bar{t} + g(t) \, \mathrm{d}\bar{\mathbf{w}}_t \\ &= \left[\mathbf{f}(\mathbf{x}_t,t) - g^2(t) \left(\nabla \log p_r^t - \nabla \log \frac{d_{\phi_*}}{1 - d_{\phi_*}} + \nabla \log \frac{d_{\phi}}{1 - d_{\phi}}\right)\right] \mathrm{d}\bar{t} + g(t) \, \mathrm{d}\bar{\mathbf{w}}_t. \end{split}$$

Applying the Girsanov theorem to this generative SDE with the reverse-time data SDE with the data-processing inequality, we get

$$D_{KL}(p_r \| p_{\theta, \phi}) \le D_{KL}(p_r^T \| \pi) + \frac{1}{2} \int_0^T g^2(t) \mathbb{E}_{p_r^t} \left[ \left\| \nabla \log \frac{d_{\phi_*}}{1 - d_{\phi_*}} - \nabla \log \frac{d_{\phi}}{1 - d_{\phi}} \right\|_2^2 \right] dt.$$

Also, the equality of  $D_{KL}(p_r \| p_{\theta}) = D_{KL}(p_r^T \| \pi) + \frac{1}{2} \int_0^T g^2(t) \mathbb{E}_{p_r^t} \left[ \|\nabla \log p_r^t - \nabla \log p_{\theta}^t \|_2^2 \right] dt$  holds by Lemma 2.  $\square$ 

#### A.3. Validity of Assumption in Theorem 1

It now remains to show if the assumptions of Theorem 1 holds in practice. Figure 13 compares the NLL and NELBO curve of  $s_{\theta_{\infty}}$ . Figure 13 shows that the equality condition of NLL and NELBO holds approximately on a wide range of time horizon, in practice.

Figure 13 is obtained from the EDM checkpoint (Karras et al., 2022). For the NLL and NELBO computation, we follow Kim et al. (2022a;b): we estimate the truncated NLL and NELBO for the purpose of thorough investigation throughout timescales. The truncated NLL and NELBO assumes that the score network is given only on  $(\tau,T]$  with  $\tau$  a truncation bound. Then, the truncated NLL is the right-hand-side of

truncated NLL between 
$$(\tau,T]$$

truncated NELBO between  $(\tau,T]$ 

truncated NELBO between  $(\tau,T]$ 
 $10^{-2}$ 
 $10^{-1}$ 
 $10^{0}$ 
 $10^{1}$ 
 $10^{2}$ 

Perturbation Scale  $\sigma(\tau)$ 

Figure 13: NELBO is uniformly close to NLL on CIFAR-10.

$$\mathbb{E}_{\mathbf{x}_0 \sim p_r}[-\log p_g(\mathbf{x}_0)] \leq \mathbb{E}_{\mathbf{x}_\tau \sim p_r^\tau}[-\log p_{\boldsymbol{\theta},\tau}(\mathbf{x}_\tau)] + R_\tau(\boldsymbol{\theta}),$$

where  $R_{\tau}(\boldsymbol{\theta}) = \mathbb{E}_{\mathbf{x}_0 \sim p_r} \left[ \int p_{0\tau}(\mathbf{x}_{\tau}|\mathbf{x}_0) \log \frac{p_{0\tau}(\mathbf{x}_{\tau}|\mathbf{x}_0)}{p_{\boldsymbol{\theta}}(\mathbf{x}_0|\mathbf{x}_{\tau})} d\mathbf{x}_{\tau} \right]$  and  $p_{\boldsymbol{\theta},\tau}$  is the marginal density at  $\tau$  of the generative process. We evaluate  $p_{\boldsymbol{\theta},\tau}(\mathbf{x}_{\tau})$  by solving the instantaneous change-of-variable formula

$$\frac{\mathrm{d}}{\mathrm{d}t}\log p_{\boldsymbol{\theta},t}(\mathbf{x}_t) = -\mathrm{tr}\bigg(\nabla\Big[\mathbf{f}(\mathbf{x}_t,t) - \frac{1}{2}g^2(t)\mathbf{x}_{\boldsymbol{\theta}}(\mathbf{x}_t,t)\Big]\bigg)$$

from  $t = \tau$  to T, of which probability flow ODE is

$$d\mathbf{x}_t = \left[\mathbf{f}(\mathbf{x}_t, t) - \frac{1}{2}g^2(t)\mathbf{s}_{\theta}(\mathbf{x}_t, t)\right]dt.$$

Analogously, we evaluate the truncated evidence lower bound as the right-hand-side of

$$\mathcal{L}([0,T]) \leq \mathcal{L}([\tau,T]) + R_{\tau}(\boldsymbol{\theta}),$$

where

$$\mathcal{L}([\tau, T]) = \frac{1}{2} \int_{\tau}^{T} \mathbb{E}\left[g^{2}(t) \|\nabla \log p_{0t}(\mathbf{x}_{t}|\mathbf{x}_{0}) - \mathbf{s}_{\boldsymbol{\theta}}(\mathbf{x}_{t}, t)\|_{2}^{2} - g^{2}(t) \|\nabla \log p_{0t}(\mathbf{x}_{t}|\mathbf{x}_{0})\|_{2}^{2} - 2\operatorname{div}(\mathbf{f})\right] dt - \mathbb{E}\left[\log \pi(\mathbf{x}_{T})\right].$$

We utilize the importance sampling technique (for the integration with respect to t in  $\mathcal{L}$ ) to minimize the estimation variance of the evidence lower bound. To derive the closed-form importance-weighted time, first, observe that the EDM forward diffusion is given by  $\sigma^2(t) = (\sigma_{min}^{1/\rho} + t(\sigma_{max}^{1/\rho} - \sigma_{min}^{1/\rho}))$ . Then, with the importance weight of  $\frac{g^2(t)}{\sigma^2(t)}$ , if we define  $F(t) = \frac{1}{Z} \int_{\tau}^{t} \frac{g^2(s)}{\sigma^2(s)} \, \mathrm{d}s$  to be the cumulative distribution function of the importance sampler, the importance-weighted time becomes  $t = F^{-1}(u)$  for uniformly sampled u on [0, T].

Now, the antiderivative of the importance weight becomes

$$\mathcal{F}(t) = \int \frac{g^{2}(t)}{\sigma^{2}(t)} dt$$

$$= \int 2\rho \frac{\sigma_{max}^{1/\rho} - \sigma_{min}^{1/\rho}}{\sigma_{min}^{1/\rho} + t(\sigma_{max}^{1/\rho} - \sigma_{min}^{1/\rho})} dt$$

$$= 2\rho \log (\sigma_{min}^{1/\rho} + t(\sigma_{max}^{1/\rho} - \sigma_{min}^{1/\rho})),$$

and the normalizing constant becomes

$$Z = \int_{\tau}^{T} \frac{g^{2}(t)}{\sigma^{2}(t)} dt$$

$$= \mathcal{F}(T) - \mathcal{F}(\tau)$$

$$= 2\rho \log \frac{\sigma_{min}^{1/\rho} + T(\sigma_{max}^{1/\rho} - \sigma_{min}^{1/\rho})}{\sigma_{min}^{1/\rho} + \tau(\sigma_{max}^{1/\rho} - \sigma_{min}^{1/\rho})}.$$

Therefore, we have

$$t = F^{-1}(u)$$

$$\iff u = F(t) = \frac{1}{Z} \int_{\tau}^{t} \frac{g^{2}(s)}{\sigma^{2}(s)} ds = \frac{1}{Z} \left( \mathcal{F}(t) - \mathcal{F}(\tau) \right)$$

$$\iff u \log \frac{\sigma_{min}^{1/\rho} + T(\sigma_{max}^{1/\rho} - \sigma_{min}^{1/\rho})}{\sigma_{min}^{1/\rho} + \tau(\sigma_{max}^{1/\rho} - \sigma_{min}^{1/\rho})} = \log \frac{\sigma_{min}^{1/\rho} + t(\sigma_{max}^{1/\rho} - \sigma_{min}^{1/\rho})}{\sigma_{min}^{1/\rho} + \tau(\sigma_{max}^{1/\rho} - \sigma_{min}^{1/\rho})}$$

$$\iff \left( \frac{\sigma_{min}^{1/\rho} + T(\sigma_{max}^{1/\rho} - \sigma_{min}^{1/\rho})}{\sigma_{min}^{1/\rho} + \tau(\sigma_{max}^{1/\rho} - \sigma_{min}^{1/\rho})} \right)^{u} = \frac{\sigma_{min}^{1/\rho} + t(\sigma_{max}^{1/\rho} - \sigma_{min}^{1/\rho})}{\sigma_{min}^{1/\rho} + \tau(\sigma_{max}^{1/\rho} - \sigma_{min}^{1/\rho})}$$

$$\iff \left( \sigma_{min}^{1/\rho} + \tau(\sigma_{max}^{1/\rho} - \sigma_{min}^{1/\rho}) \right) \left( \frac{\sigma_{min}^{1/\rho} + T(\sigma_{max}^{1/\rho} - \sigma_{min}^{1/\rho})}{\sigma_{min}^{1/\rho} + \tau(\sigma_{max}^{1/\rho} - \sigma_{min}^{1/\rho})} \right)^{u} = \sigma_{min}^{1/\rho} + t(\sigma_{max}^{1/\rho} - \sigma_{min}^{1/\rho})$$

$$\iff t = \left( \left( \sigma_{min}^{1/\rho} + \tau(\sigma_{max}^{1/\rho} - \sigma_{min}^{1/\rho}) \right) \left( \frac{\sigma_{min}^{1/\rho} + T(\sigma_{max}^{1/\rho} - \sigma_{min}^{1/\rho})}{\sigma_{min}^{1/\rho} + \tau(\sigma_{max}^{1/\rho} - \sigma_{min}^{1/\rho})} \right)^{u} - \sigma_{min}^{1/\rho} \right) / (\sigma_{max}^{1/\rho} - \sigma_{min}^{1/\rho}).$$

## A.4. Why $p_{m{ heta}}^t$ is defined as a forward marginal rather than a generative marginal

Unintuitively, we define  $p_{\theta}^t$  as a forward-time marginal density rather than a reverse-time generative marginal. We design  $p_{\theta}^t$  as a forward-time marginal by two reasons. First, it saves memory. If it was the reverse-time generative marginal, the generated dataset  $\mathcal{G}$  should contain the whole sample trajectories to optimize the time-embedded discriminator, and this

could be prohibitive when we run  $\sim 1000$  steps to generate a sample. Instead, if we use the forward-time marginal, we could only save the final sample as  $\mathcal{G}$ , and we optimize the discriminator by diffusing it with *arbitrary* diffusion time with *arbitrary* diffusion noise. Here comes the second advantage: as we could update the discriminator with arbitrary diffusion noise, it attains the data augmentation effect in training the discriminator network, and it could prevent the overfitting issue at large time. On the other hand, if it was the generative marginal, the discriminator guidance needs more sample data to prevent overfitting.

## **B.** More on Bregman Divergences

The most general framework for learning the density-ratio  $\frac{p_p^t}{p_\theta^t}$  is using the Bregman divergence (Sugiyama et al., 2012). In this section, we investigate the effect of representative Bregman divergences. To begin with, let us define the Bregman divergence in an abstract form. Suppose  $r^*(\mathbf{x}) = \frac{p_{nu}(\mathbf{x})}{p_{de}(\mathbf{x})}$  be the target density-ratio to be estimated with  $r_{\phi}$ , parametrized by  $\phi$ . Then,

$$D_h(r^* || r_{\phi}) = \int p_{de}(\mathbf{x}) B_h(r^*(\mathbf{x}) || r_{\phi}(\mathbf{x})) d\mathbf{x}$$
$$= \int p_{de}(\mathbf{x}) \Big( h(r^*(\mathbf{x})) - h(r_{\phi}(\mathbf{x})) - \partial h(r_{\phi}(\mathbf{x})) (r^*(\mathbf{x}) - r_{\phi}(\mathbf{x})) \Big) d\mathbf{x},$$

where  $B_h$  is the data-level Bregman divergence. For a twice continuously differentiable convex function h with a bounded derivative  $\partial h$ , the Bregman divergence quantifies the discrepancy between two density-ratios. Subtracting a constant term  $\int p_{de}(\mathbf{x})h(r^*(\mathbf{x})) \,\mathrm{d}x$ , we obtain (up to a constant)

$$D_h(r^*||r_{\phi}) = \int p_{de}(\mathbf{x}) \Big[ \partial h \big( r_{\phi}(\mathbf{x}) \big) r_{\phi}(\mathbf{x}) - h \big( r_{\phi}(\mathbf{x}) \big) \Big] d\mathbf{x} - \int p_{nu}(\mathbf{x}) \Big[ \partial h \big( r_{\phi}(\mathbf{x}) \big) \Big] d\mathbf{x}.$$

A few non-exhaustive examples of the Bregman divergence are Least-Squared Importance Fitting (LSIF) (Kanamori et al., 2009), Binary Cross Entropy (BCE) (Hastie et al., 2009), and Kullback-Leibler Importance Estimation Procedure (KLIEP) (Nguyen et al., 2010). LSIF is equivalent to

$$BD_{f_{LSIF}}(r^*||r_{\phi}) = \frac{1}{2} \int p_{de}(\mathbf{x}) (r^*(\mathbf{x}) - r_{\phi}(\mathbf{x}))^2 d\mathbf{x}$$
$$= \frac{1}{2} \int p_{de}(\mathbf{x}) r_{\phi}^2(\mathbf{x}) d\mathbf{x} - \int p_{nu}(\mathbf{x}) r_{\phi}(\mathbf{x}) d\mathbf{x},$$

with  $h_{LSIF}(r) = (r-1)^2/2$ . BCE is also widely denoted as Binary Kullback-Leibler (BKL), and is defined with  $h_{BKL}(r) = r \log r - (1+r) \log (1+r)$ . KLIEP is also known as the Unbounded Kullback-Leibler (UKL) with  $h_{UKL}(r) = r \log r - r$ , and is a Lagrangian of the constrained optimization problem of

$$D_{KL}(p_{nu}||p_{nu,\phi})$$
 subject to  $\int p_{nu,\phi}(\mathbf{x}) d\mathbf{x} = 1$ ,

where  $p_{nu,\phi}(\mathbf{x}) := p_{de}(\mathbf{x})r_{\phi}(\mathbf{x})$ . The UKL Bregman divergence is defined as the Lagrangian of the above problem by

$$BD_{f_{UKL}}(r^*||r_{\phi}) = \int p_{de}(\mathbf{x})r_{\phi}(\mathbf{x}) d\mathbf{x} - \int p_{nu}(\mathbf{x}) \log r_{\phi}(\mathbf{x}) d\mathbf{x}.$$

Now, we consider the time-dependent Bregman divergence to train the discriminator network. The time-dependent Bregman divergence is defined by

$$\int \lambda(t) D_h \left( \frac{p_r^t(\cdot)}{p_{\boldsymbol{\theta}}^t(\cdot)} \left\| \frac{1 - d_{\boldsymbol{\phi}}(\cdot, t)}{d_{\boldsymbol{\phi}}(\cdot, t)} \right) dt,$$

where  $\lambda(t)$  is a time-weighting function. We train the discriminator network with this time-dependent Bregman divergence of LSIF, BCE, and UKL. In a toy 2-dimensional case, Figures 15 and 14 visualizes the adjusted score by discriminators trained by aforementioned Bregman divergences: Figure 15 for the case where the estimated score is completely blind to the data score, and Figure 14 for the case where the estimated score is confusing on the exact location of bi-modalities of the data distribution. Figures 15 and 14 illustrate that BCE estimates the correction term  $\mathbf{c}_{\theta}$  most robust.

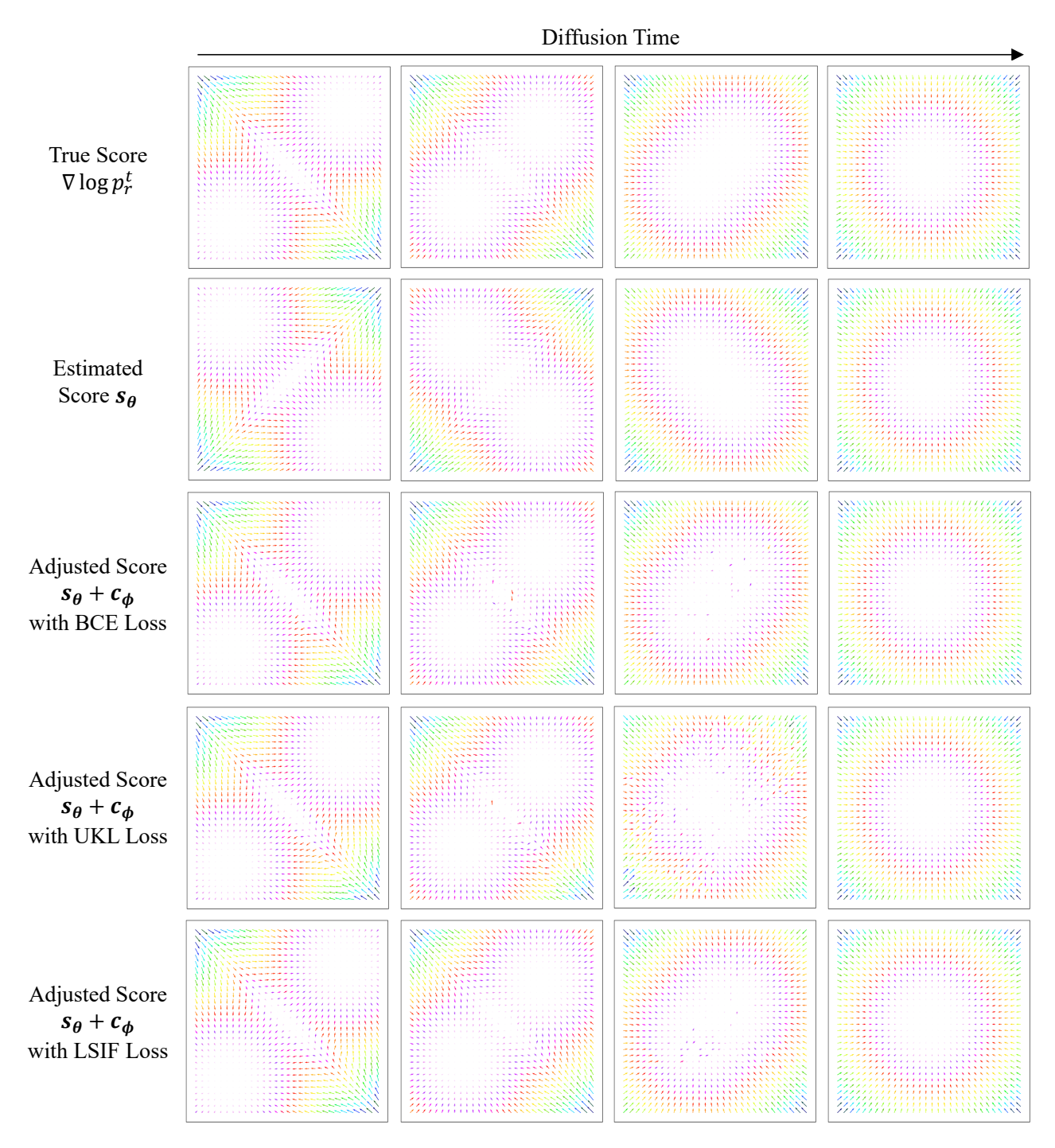


Figure 14: A 2-dimentionsal toy case with a bimodal Gaussian data distribution. In this experiment, we visualize the adjusted scores for BKL/UKL/LSIF losses under the assumption that the estimated score is misleadingly capturing the location of bimodalities.

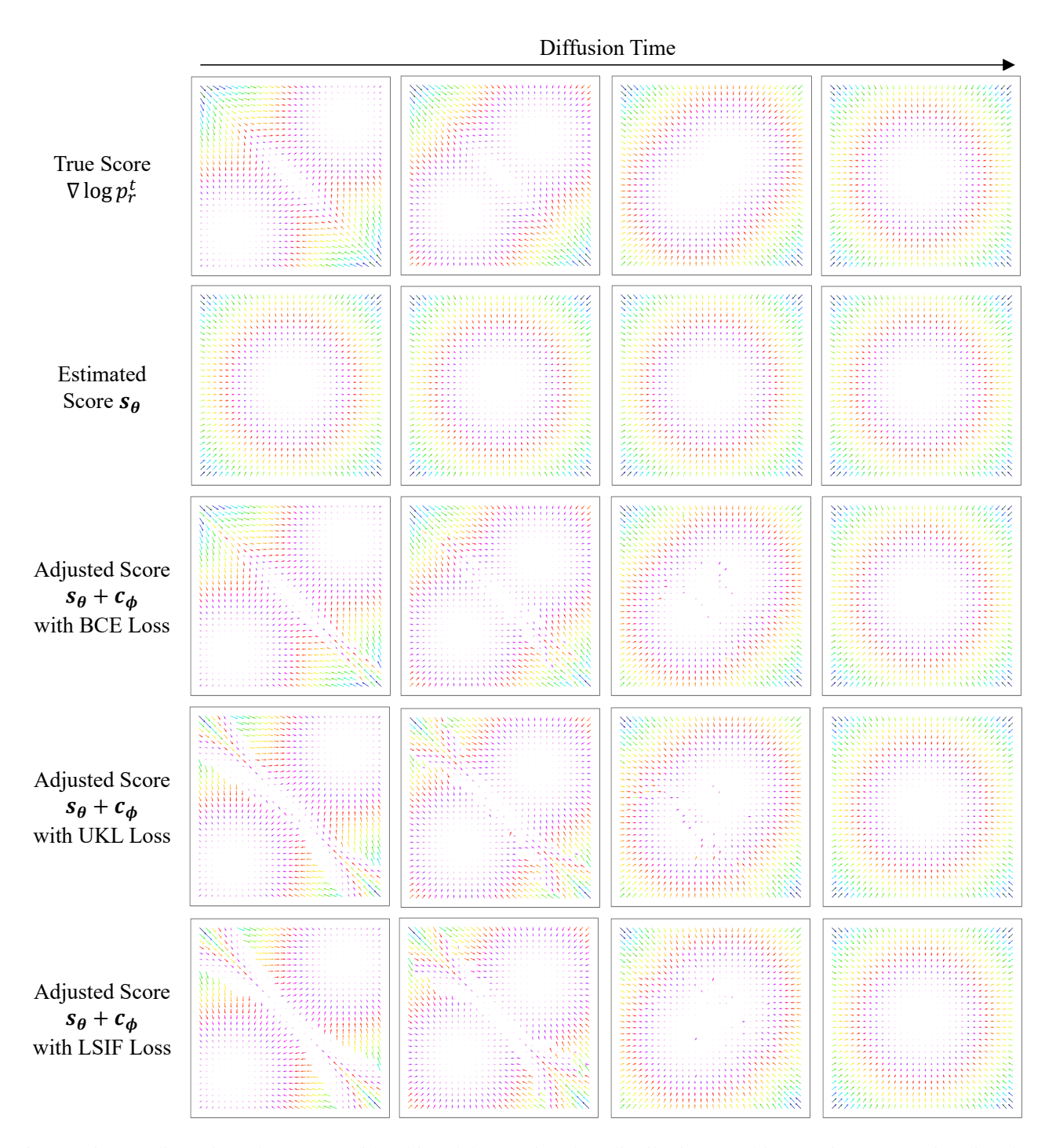
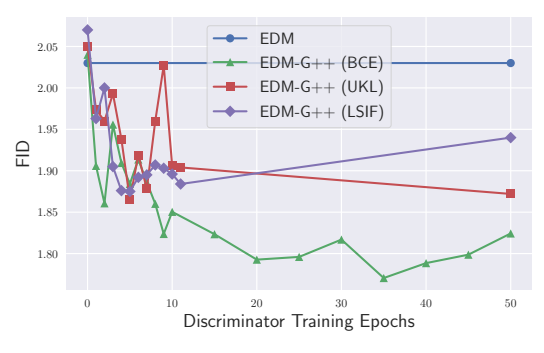
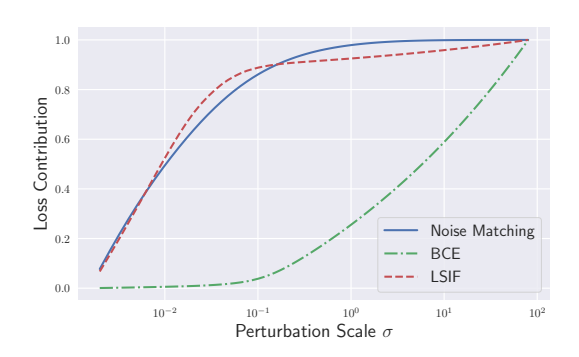


Figure 15: A 2-dimentionsal toy case with a bimodal Gaussian data distribution. In this experiment, we visualize the adjusted scores for BKL/UKL/LSIF losses under the assumption that the estimated score is completely blind to the data distribution, which means that the estimated score  $s_{\theta}$  is simply a score function of a standard Gaussian distribution.





(a) FID by Discriminator Training

(b) Loss Contribution

Figure 16: Study of EDM on CIFAR-10 with respect to Bregman divergences. (a) illustrates how sample quality is improved by discriminator training with various loss functions, and (b) shows the mechanism of such different FID.

Figure 16-(a) shows that the listed divergences have distinctive characteristics in sample quality. Similar to the 2-dimensional case, BCE performs the best. Figure 16-(b) illustrates why such a behavioral difference occurs. We visualize the (normalized) cumulative loss to the perturbation scale. For the noise matching, most loss contribution is on the range of small diffusion scale (Kim et al., 2022b). On the contrary, BCE is qualitatively different from the score loss: most of loss is concentrated on the range of large diffusion scale, and it would be presumably the reason for the arguments in Section 6. Figure 16-(b) shows that LSIF is similar to the noise matching loss. For the UKL loss, we do not plot the cumulative loss because the loss is neither strictly positive nor strictly negative for every diffusion scale.

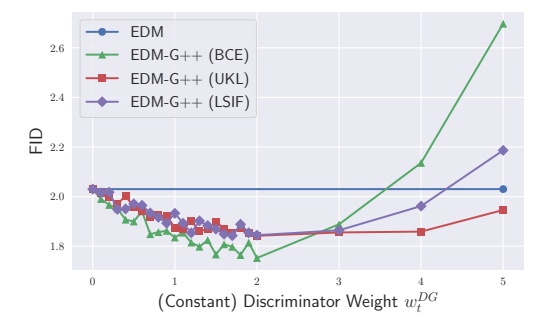


Figure 17: Study of  $w_t^{DG}$  for various Bregman divergences on CIFAR-10.

Figure 17 conducts the ablation study of  $w_t^{DG}$  for various Bregman divergences on CIFAR-10. It illustrates that BCE loss performs the best but UKL loss is the most robust one.

## C. Details on Image-to-Image Translation

Figure 18 illustrates the step-by-step denoising process of I2I translation task. Suppose  $\mathbf{x}_0 \sim \mathcal{S}$  is the source image, and  $\mathbf{y}_0 \sim \mathcal{T}$  is the target image. Then, following SDEdit (Meng et al., 2021), we start denoising from  $\mathbf{x}_{\tau}$  with

$$d\mathbf{y}_t = [\mathbf{f}(\mathbf{y}_t, t) - g^2(t)\mathbf{s}_{\theta}(\mathbf{y}_t, t)] d\bar{t} + g(t) d\bar{\mathbf{w}}_t,$$

where  $\mathbf{s}_{\theta}(\mathbf{y}_t,t)$  is the score network trained on the target domain. Suppose we define  $\mathbf{z}_{\theta}^t$  be the random variable of the solution process:  $\mathbf{z}_{\theta}^{t_{mid}} = \mathbf{x}_{t_{mid}}$  is the starting variable and  $\mathbf{z}_{\theta}^0$  is the translated variable. Suppose  $q_{\theta}^t$  be the probability distribution of  $\mathbf{z}_{\theta}^t$ ,  $p_{\theta} = q_{\theta}^0$  be the probability distribution of  $\mathbf{z}_{\theta}^t$ , and  $p_{\theta}^t$  be the probability distribution of the diffused variable by the forward SDE, starting from  $\mathbf{z}_{\theta}^0$ . For the discriminator training, we sample  $\mathbf{z}_t \sim \alpha p_{\mathcal{S}}^t(\mathbf{z}_t) + (1-\alpha)p_{\theta}^t(\mathbf{z}_t)$  for the fake data and  $\mathbf{y}_t \sim p_{\mathcal{T}}^t(\mathbf{y}_t)$  for the real data. Then, our discriminator guidance becomes

$$d\mathbf{y}_{t} = \left[\mathbf{f}(\mathbf{y}_{t}, t) - g^{2}(t) \left(\mathbf{s}_{\theta}(\mathbf{y}_{t}, t) + \nabla \log \frac{p_{\mathcal{T}}^{t}(\mathbf{y}_{t})}{\alpha p_{\mathcal{S}}^{t}(\mathbf{y}_{t}) + (1 - \alpha) p_{\theta}^{t}(\mathbf{y}_{t})}\right)\right] d\bar{t} + g(t) d\bar{\mathbf{w}}_{t}.$$

When  $t \approx t_{mid}$ , we have  $p_S^t(\mathbf{z}_t) \gg p_{\theta}^t(\mathbf{z}_t)$  for  $\mathbf{z}_t \sim q_{\theta}^t$  and the adjusted generative process is approximately

$$d\mathbf{y}_{t} \approx \left[\mathbf{f}(\mathbf{y}_{t}, t) - g^{2}(t) \left(\mathbf{s}_{\theta}(\mathbf{y}_{t}, t) + \nabla \log \frac{p_{\mathcal{T}}^{t}(\mathbf{y}_{t})}{p_{\mathbf{s}}^{t}(\mathbf{y}_{t})}\right)\right] d\bar{t} + g(t) d\bar{\mathbf{w}}_{t},$$

so the discriminator guidance gives a direct signal to avoid from  $p_{\mathcal{S}}^t$  when  $t \approx t_{mid}$ . When  $t \approx 0$ , we have  $p_{\mathcal{S}}^t(\mathbf{z}_t) \ll p_{\theta}^t(\mathbf{z}_t)$  for  $\mathbf{z}_t \sim q_{\theta}^t$  and the adjusted generative process is approximately

$$d\mathbf{y}_{t} \approx \left[\mathbf{f}(\mathbf{y}_{t}, t) - g^{2}(t) \left(\mathbf{s}_{\theta}(\mathbf{y}_{t}, t) + \nabla \log \frac{p_{\mathcal{T}}^{t}(\mathbf{y}_{t})}{p_{\theta}^{t}(\mathbf{y}_{t})}\right)\right] d\bar{t} + g(t) d\bar{\mathbf{w}}_{t},$$

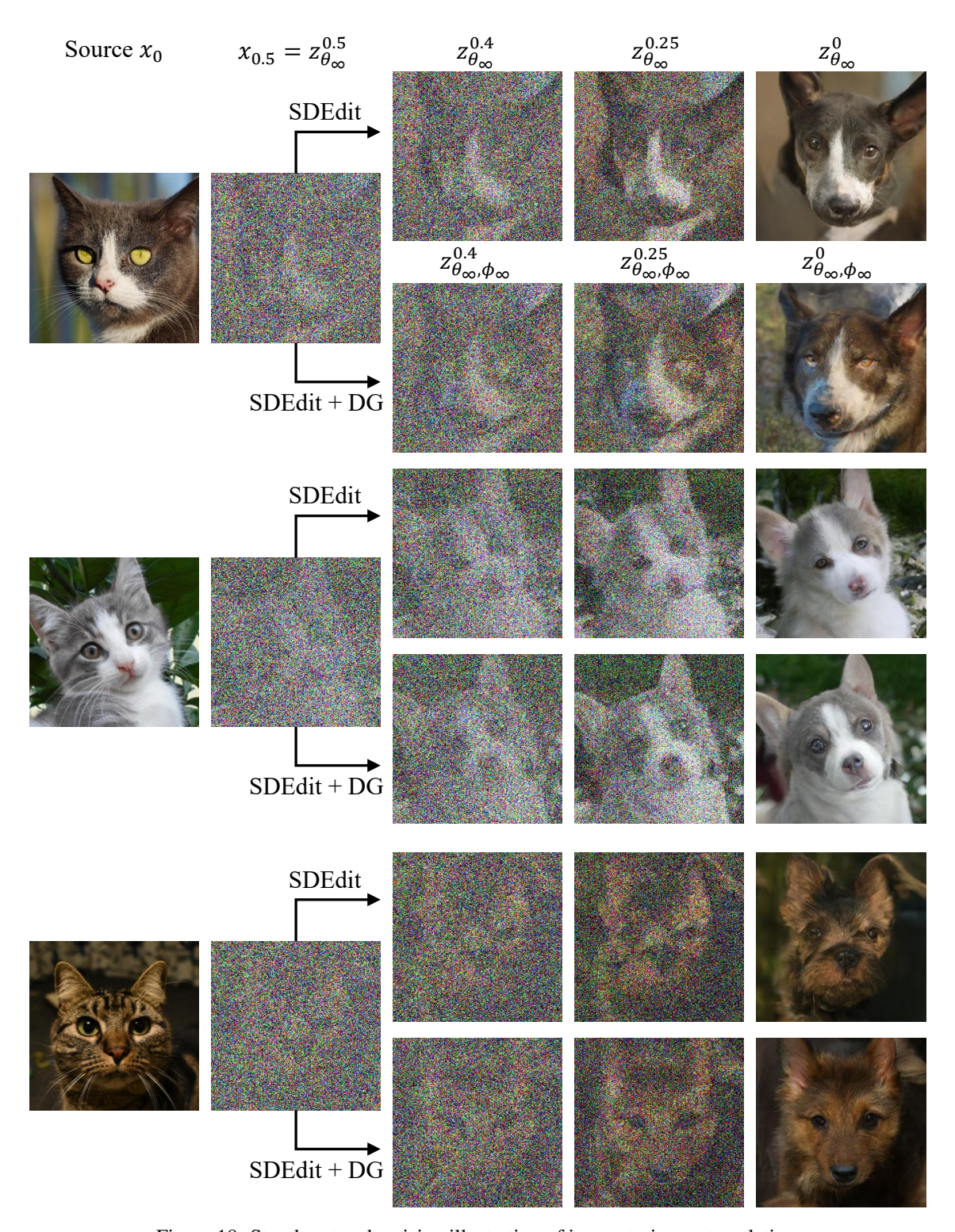


Figure 18: Step-by-step denoising illustration of image-to-image translation.

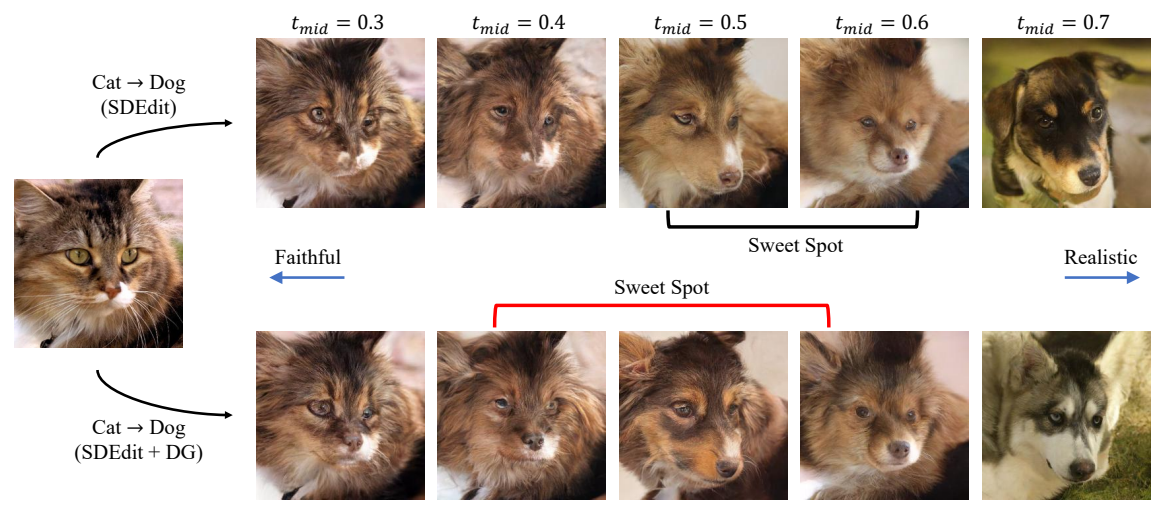


Figure 19: The discriminator guidance swifts the sweet spot to the range of small  $t_0$ .

and the discriminator is guiding the sample denoising toward the desired destination density  $p_{\mathcal{T}}^t$ , rather than the original destination density  $p_{\theta}^t$ .

By applying the discriminator guidance, more realistic samples are generated with relatively small  $t_{mid}$ , compared to SDEdit, so we could lift the sweet spot of the image-to-image translation to a range of small  $t_{mid}$  as in Figure 19.

### **D.** Experimental Details

#### D.1. Training and Sampling Details

Table 8 presents the experimental configuration for Tables 2, 3, and 4. Except for ImageNet 256x256, we solve the Probability-Flow ODE (PFODE) (Song et al., 2020b) for sampling. We use the adjusted PFODE

$$\frac{\mathrm{d}\mathbf{x}_t}{\mathrm{d}t} = \mathbf{f}(\mathbf{x}_t, t) - \frac{1}{2}g^2(t)(\mathbf{s}_{\theta_{\infty}} + w_t^{DG}\mathbf{c}_{\phi_{\infty}})(\mathbf{x}_t, t)$$

on  $t \in [t_{mid}, T]$  and the unadjusted PFODE

$$\frac{\mathrm{d}\mathbf{x}_t}{\mathrm{d}t} = \mathbf{f}(\mathbf{x}_t, t) - \frac{1}{2}g^2(t)\mathbf{s}_{\boldsymbol{\theta}_{\infty}}(\mathbf{x}_t, t)$$

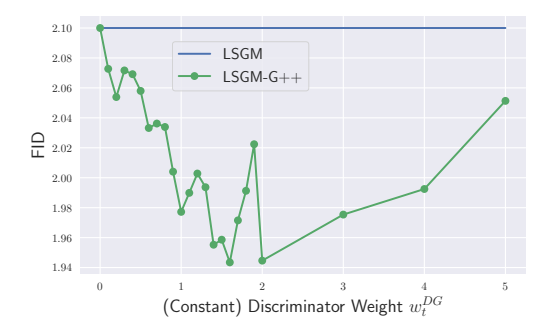


Figure 20: Ablation of  $\boldsymbol{w}_t^{DG}$  in LSGM-G++ on CIFAR-10.

on  $t \in [0, t_{mid}]$ .

For LSGM-G++, we borrow the pre-trained CIFAR-10 checkpoint of LSGM with best FID (Vahdat et al., 2021) at https://github.com/NVlabs/LSGM. We do not use any of the pre-trained classifier for this latent-diffusion model, and we train a discriminator from scratch. We solve the unadjusted/adjusted PFODEs with explicit Runge-Kutta solver of order 5(4) (Dormand & Prince, 1980). We find  $w_t^{DG}=2$  works the best in practice and report the value in Table 2. Figure 20 presents the ablation study on DG weight.

For EDM-G++, we experiment with unconditional and conditional CIFAR-10, as well as FFHQ 64x64. We use the pre-trained score model of EDM (Karras et al., 2022) at https://github.com/NVlabs/edm. For the classifier, we borrow a pre-trained classifier from ADM (Dhariwal & Nichol, 2021) at https://github.com/openai/guided-diffusion on 64x64 FFHQ, and we train a 32x32 classifier (and freeze it at discriminator training phase) for CIFAR-10 experiment. We use the ImageNet dataset (Russakovsky et al., 2015) to train the 32x32 classifier. We follow the identical setting of Dhariwal & Nichol (2021) to train the 32x32 classifier, except the dataset resolution. We solve the unadjusted/adjusted PFODEs with a Heun solver (Ascher & Petzold, 1998) with pre-designated timesteps that is determined by NFE. As the Heun solver is a  $2^{\rm nd}$ -order numerical solver, we divide the DG weight  $w_t^{\rm DG}$  into  $w_{t,1^{\rm st}}^{\rm DG}$  and  $t_{t,2^{\rm nd}}^{\rm DG}$ , where  $w_{t,1^{\rm st}}^{\rm DG}$  is for the

Table 8: Training and sampling configurations.

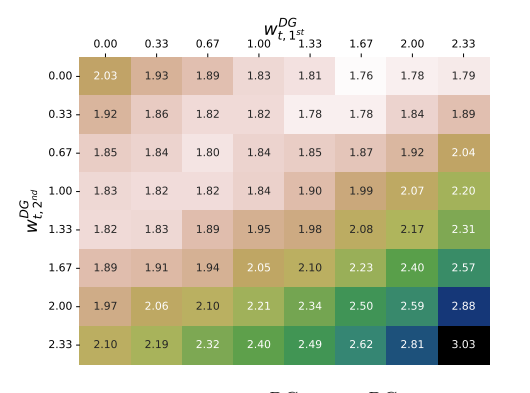
		CIFAR-10		CelebA	FFHQ	ImageNet256	
	LSGM-G++	EDM	-G++	STDDPM-G++	EDM-G++	ADM-G++	
Pre-trained Score Network							
Model	LSGM	EDM	EDM	STDDPM	EDM	ADM	
Class condition	Х	X	✓	Х	Х	✓	
Discriminator Training							
SDE	LVP	LVP	LVP	CVP	CVP	LVP	
Class condition	X	X	✓	X	X	✓	
Time sampling	Importance	Importance	Importance	Importance	Importance	Importance	
$\lambda$	$\frac{g^2}{\sigma^2}$	$\frac{g^2}{\sigma^2}$	$\frac{g^2}{\sigma^2}$	$10^{\frac{g^2}{\sigma^2}}$	$\frac{g^2}{\sigma^2}$	$\frac{g^2}{\sigma^2}$	
Minimum diffusion time	0.01	$10^{-5}$	$10^{-5}$	$10^{-5}$	$10^{-5}$	$10^{-5}$	
EMA	<b>X</b>	×	×	×	×	X	
Batch size	128	128	128	128	128	512	
$\#\mathcal{D}$	50,000	50,000	50.000	10.000	60.000	1,281,167	
# <i>G</i>	50,000	25,000	50,000	10.000	60.000	400,000	
# Epochs	280	60	250	150	250	10	
GPUs	1x V100	1x V100	1x V100	1x V100	1x V100	1x A100	
Pre-trained Classifier							
Model	No classifier	ADM	ADM	ADM	ADM	ADM	
Input shape (data dimension)	X	(B,32,32,3)	(B,32,32,3)	(B,64,64,3)	(B,64,64,3)	(B,256,256,3)	
Output shape (latent dimension)	x	(B,8,8,512)	(B,8,8,512)	(B,8,8,512)	(B,8,8,512)	(B,8,8,512)	
		(B,0,0,312)	(B,0,0,312)	(B,0,0,312)	(B,0,0,312)	(B,0,0,312)	
Shallow U-Net Architecture	· · · · · · · · · · · · · · · · · · ·	~		~ ~ ~ ~ ~ ~ ~			
Input shape (latent dimension)	(B,16,16,180)	(B,8,8,512)	(B,8,8,512)	(B,8,8,512)	(B,8,8,512)	(B,8,8,512)	
Output shape	(B,1)	(B,1)	(B,1)	(B,1)	(B,1)	(B,1)	
Minimum value of discriminator (clip)	$10^{-5}$	0	0	0	0	$10^{-5}$	
Maximum value of discriminator (clip)	$1 - 10^{-5}$	1	1	1	1	$1 - 10^{-5}$	
Class condition	X	X	✓.	X	X	✓.	
# Resnet blocks	5	4	4	6	6	4	
# Attention blocks	3	3	3	5	5	3	
Attention resolutions	16, 8	8	8	8	8	8	
Model channel	128	128	128	128	128	128	
Channel multiplier	(1,2)	1	1	1	1	1	
Sampling							
SDE	LVP	WVE	WVE	LVP	WVE	LVP	
Class condition	×	X _	✓ _	X	X	✓ _	
Minimum value of discriminator (clip)	$10^{-3}$	$10^{-5}$	$10^{-5}$	$10^{-5}$	$10^{-5}$	$10^{-5}$	
Maximum value of discriminator (clip)	$1 - 10^{-3}$	$1-10^{-5}$	$1 - 10^{-5}$	$1 - 10^{-5}$	$1 - 10^{-5}$	$1 - 10^{-5}$	
Solver	PFODE	PFODE	PFODE	PFODE	PFODE	DDPM	
Solver accuracy of $s_{\theta}$	1st-order	2 <sup>nd</sup> -order	2 <sup>nd</sup> -order	1st-order	2 <sup>nd</sup> -order	1st-order	
Solver type of $s_{\theta}$	RK45	Heun	Heun	RK45	Heun	Euler (DDPM)	
Solver accuracy of $\mathbf{c}_{\phi}$	1st-order	1st-order	1st-order	1st-order	1st-order	1st-order	
Solver type of $\mathbf{c}_{\phi}$	RK45	Euler	Euler	RK45	Euler	Euler	
$t_{mid}$	0.1	0.01	0.01	0.01	0.01	0.1	
NFE	138	35	35	131	71	250	
Classifier Guidance	×	X	X	X	X	✓	
EDS	×	×	×	X	×	✓	
$w_t^{CG}$	0	0	0	0	0	Adaptive	
$egin{array}{c} w_t^{CG} \ w_t^{DG} \end{array}$	2	2	Adaptive	Adaptive	Adaptive	Adaptive	

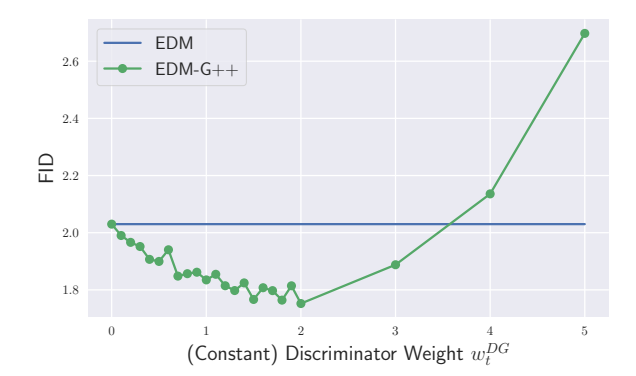
 $1^{\mathrm{st}}$ -order and  $t_{t,2^{\mathrm{nd}}}^{DG}$  is for the  $2^{\mathrm{nd}}$ -order. For denoising, we construct an intermediate state

$$\tilde{\mathbf{x}}_{t-\Delta t} = \mathbf{x}_t - \Delta t \Big[ f(\mathbf{x}_t, t) - \frac{1}{2} g^2(t) (\mathbf{s}_{\theta_{\infty}} + w_{t, 1^{\text{st}}}^{DG} \mathbf{c}_{\phi_{\infty}}) (\mathbf{x}_t, t) \Big].$$

Then, we denoise  $x_t$  by

$$\begin{split} \mathbf{x}_{t-\Delta t} &= \mathbf{x}_t - \Delta t \left[ \frac{1}{2} \Big( \mathbf{f}(\mathbf{x}_t, t) - \frac{1}{2} g^2(t) (\mathbf{s}_{\boldsymbol{\theta}_{\infty}} + w_{t, 1^{\text{st}}}^{DG} \mathbf{c}_{\boldsymbol{\phi}_{\infty}}) (\mathbf{x}_t, t) \Big) \right. \\ &\quad + \frac{1}{2} \Big( \mathbf{f}(\tilde{\mathbf{x}}_{t-\Delta t}, t - \Delta t) - \frac{1}{2} g^2(t - \Delta t) (\mathbf{s}_{\boldsymbol{\theta}_{\infty}} + w_{t, 2^{\text{nd}}}^{DG} \mathbf{c}_{\boldsymbol{\phi}_{\infty}}) (\tilde{\mathbf{x}}_{t-\Delta t}, t - \Delta t) \Big) \right] \\ &= \mathbf{x}_t - \Delta t \left[ \frac{1}{2} \Big( \mathbf{f}(\mathbf{x}_t, t) + \mathbf{f}(\tilde{\mathbf{x}}_{t-\Delta t}, t - \Delta t) \Big) - \frac{1}{4} \Big( g^2(t) \mathbf{s}_{\boldsymbol{\theta}_{\infty}}(\mathbf{x}_t, t) + \mathbf{s}_{\boldsymbol{\theta}_{\infty}}(\tilde{\mathbf{x}}_{t-\Delta t}, t - \Delta t) \Big) - \frac{1}{4} \Big( w_{t, 1^{\text{st}}}^{DG} g^2(t) \mathbf{c}_{\boldsymbol{\phi}_{\infty}}(\mathbf{x}_t, t) + w_{t, 1^{\text{nd}}}^{DG} g^2(t - \Delta t) \mathbf{c}_{\boldsymbol{\phi}_{\infty}}(\tilde{\mathbf{x}}_{t-\Delta t}, t - \Delta t) \Big] \,. \end{split}$$

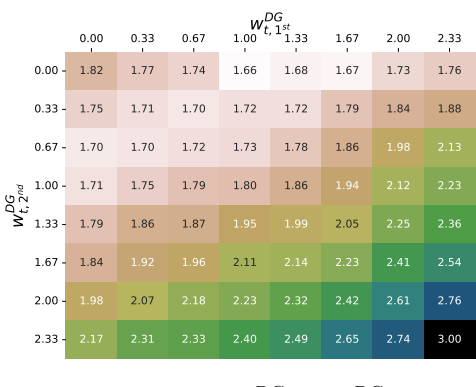


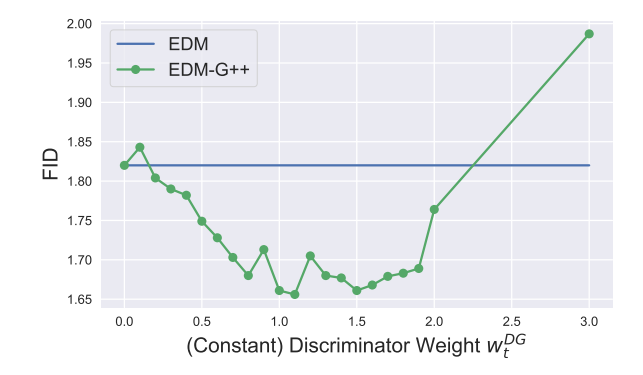


(a) Ablation of  $w_{t,1}^{DG}$  and  $w_{t,2}^{DG}$ 

(b) Detailed ablation of  $w_{t,1}^{DG}$ 

Figure 21: Study of Heun solver for EDM on unconditional CIFAR-10.





(a) Ablation of  $w_{t,1^{\text{st}}}^{DG}$  and  $w_{t,2^{\text{nd}}}^{DG}$ 

(b) Detailed ablation of  $w_{t,1^{\rm st}}^{DG}$ 

Figure 22: Study of Heun solver for EDM on conditional CIFAR-10.

Figure 21-(a) illustrates the FID heatmap with respect to  $w_{t,1^{\rm st}}^{DG}$  and  $w_{t,2^{\rm nd}}^{DG}$ . It shows that the effect of  $w_{t,1^{\rm st}}^{DG}$  is inverse proportional to that of  $w_{t,2^{\rm nd}}^{DG}$ . Also, the line  $w_{t,1^{\rm st}}^{DG}+w_{t,2^{\rm nd}}^{DG}=2$  performs the best, which is consistent to our intuition. In particular, we emphasize that the best performance happens at  $(w_{t,1^{\rm st}}^{DG},w_{t,2^{\rm nd}}^{DG})=(1.67,0)$ , which implies that DG does not has to be applied on the  $2^{\rm nd}$ -order correction stage of the Heun solver. This reduces the computational burden of calculating  $\mathbf{c}_{\phi_{\infty}}(\tilde{\mathbf{x}}_{t-\Delta t},t-\Delta t)$  at every denoising step. Figure 21-(b) shows the detailed abalation with respect to  $w_{t,1^{\rm st}}^{DG}$  with  $w_{t,2^{\rm nd}}^{DG}=0$ . From Figure 21-(b), we set  $w_{t,1^{\rm st}}^{DG}=2$  and  $w_{t,2^{\rm nd}}^{DG}=0$  by default for the Heun solver. From Figure 21, we denote  $w_{t,1^{\rm st}}^{DG}$  by  $w_{t}^{DG}$  if no confusion arises.

Similar to the unconditional CIFAR-10, conditional CIFAR-10 has a powerful FID improvement. The optimal weight strategy is at  $(w_{t,1^{\text{st}}}^{DG}, w_{t,2^{\text{nd}}}^{DG}) = (1,0)$  from Figure 22-(a), and it has FID gain of 1.66. Figure 22-(b) ablates  $w_{t,1^{\text{st}}}^{DG}$  with a fixed  $w_{t,2^{\text{nd}}}^{DG} = 0$ . The best performance is 1.66 when  $w_{t,1^{\text{st}}}^{DG} = 1.1$ . However, if we give  $w_{t,1^{\text{st}}}^{DG} = 2$  for samples with density-ratio less than 0 in every odd denoising steps and apply  $w_{t,1^{\text{st}}}^{DG} = 1$  otherwise, we get a better FID of 1.64. For such samples with density-ratio less than 0 in the odd steps, we also make  $S_{churn} = 4$  to give small stochasticity to avoid local optimum points. There might be better hyperparameter settings because  $S_{churn} = 4$  is set manually without thorough investigation. We call this approach as Adaptive in Table 8.

Adaptive DG is also effective on FFHQ. With  $(w_{t,1^{\mathrm{st}}}^{DG}, w_{t,2^{\mathrm{nd}}}^{DG}) = (2,0)$ , EDM-G++ performs 2.04 in FID, but it drops to 1.98 if we apply the Adaptive DG weight of which adaptive strategy is identical to the conditional CIFAR-10 case.

It is worth to note that the score checkpoint of EDM and classifier checkpoint of ADM are trained under different diffusion strategies. The use of distinctive SDEs leads merging two pre-trained models in one sampler being infeasible. To clarify the difference of diffusion mechanisms, we define Weighted VE (WVE) SDE by  $\mathbf{x}_t \sim \mathcal{N}(\mathbf{x}_0, \sigma_{WVE}^2(t))$  with  $\sigma_{WVE}(t) = \left(\sigma_{min}^{\frac{1}{\rho}} + t(\sigma_{max}^{\frac{1}{\rho}} - \sigma_{min}^{\frac{1}{\rho}})\right)^{\rho}$  for  $\sigma_{max} = 80$  and  $\sigma_{min} = 0.002$ , which is introduced in Karras et al. (2022). On the other hand, Ho et al. (2020) introduce Linear VP (LVP) with a linear scheduling of  $\beta(t) = \beta_{min} + t(\beta_{max} - \beta_{min})$ 

Cases	Implications	$w_{t\geq t_0}^{DG}$	$w_{t < t_0}^{DG}$	$w^{CG}_{t \geq t_0}$	$w_{t < t_0}^{CG}$	$t_0$	EDS	Scaling	FID	sFID	IS	precision	recall
(a)	+ DG	0	0 1	1.5 1.5	1.5 1.5	0	X X	X X	4.59 4.18	5.25 4.81	186.70 199.94	0.82 0.82	0.52 0.53
(b)	+ EDS to CG	0	0	1.5 0.75	1.5 0.75	0	× /		4.59 4.01	5.25 5.15	186.70 217.25	0.82 0.82	0.52 0.53
(c)	+ DG on CG-EDS	0	0	0.75 0.75	0.75 0.75	0 0	-	×	4.01 3.69	5.15 4.75	217.25 215.32	0.82 0.82	0.53 0.54
(d-1)	+ Adaptive CG	1 1	1 1	0.75 0.75	0.75 1.5	0 650	-	×	3.69 3.42	4.75 4.62	215.32 239.64	0.82 0.82	0.54 0.53
(d-2)	+ Adaptive DG	1 1	1 1/0.75	0.75 0.75	1.5 1.5	650 650	1	×	3.42 3.24	4.62 4.54	239.64 235.96	0.82 0.83	0.53 0.54
(e)	Final Results	0 1 1 1/3 1/3 1/5	1/0.75 1/0.75 1/0.75 1/0.75 1/0.75 1/0.5	0.75 0.75 0.75 0.25 0.25 0.1	1.5 1.5 2.0 1.5 1.5 2	650 650 650 650 650 600		×	3.93 3.24 3.18 3.73 4.66 4.45	5.03 4.54 4.53 5.03 5.52 5.38	252.56 235.96 255.74 204.49 183.31 190.71	0.85 0.83 0.84 0.78 0.76	0.49 0.54 0.53 0.59 0.61 0.60

Table 9: Study on  $w_t^{DG}$  and  $w_t^{CG}$  in ADM-G++ on ImageNet.

and Nichol & Dhariwal (2021) propose Cosine VP (CVP) with a cosine scheduling of  $\beta(t)$ . All of EDM checkpoints are trained under WVE, and the classifier checkpoints are trained with LVP for 32x32 and CVP for 64x64. For the brevity, we only consider the case of LVP.

The key to merging two checkpoints from different diffusion strategies is observing that VE/VP-style SDEs are indeed equivalent under scale translations. Concretely, suppose  $p_t^{VE}$  and  $p_t^{VP}$  are the marginal densities of VE/VP SDEs, respectively. Then, it satisfies that  $p_t^{VE}(\mathbf{x}_t) = p_{\tau(t)}^{VP}(\nu_{\tau(t)}\mathbf{x}_t)$  for

$$\tau = \frac{-\beta_{min} + \sqrt{\beta_{min}^2 + 2(\beta_{max} - \beta_{min}) \log 1 + \sigma_{WVE}^2(t)}}{\beta_{max} - \beta_{min}},$$

$$\nu_{\tau(t)} = e^{-\frac{1}{2} \int_0^{\tau(t)} \beta(s) \, \mathrm{d}s}.$$
(9)

With this relations, we put  $(\nu_{\tau_{t_i}}\mathbf{x}_{t_i}, \tau_{t_i}) = (\nu_{\tau(t_i)}\mathbf{x}_{t_i}, \tau(t_i))$  to the discriminator at the *i*-th denoising step of our sampler in our implementation. We reflect this actual implementation in Algorithm 2.

For STDDPM-G++ with CelebA, we utilize the pre-trained score model from Kim et al. (2022b) at https://github.com/kim-dongjun/soft-truncation and the 64x64 pre-trained classifier model of ADM. We solve the unadjusted/adjusted PFODEs with explicit Runge-Kutta solver of order 5(4) (Dormand & Prince, 1980). Similar to the aforementioned checkpoint mismatch issue, we transform time to align the pre-trained classifier on CVPSDE and the pre-trained score on LVPSDE.

For ADM-G++, we apply the pre-trained checkpoint from Dhariwal & Nichol (2021) at https://github.com/openai/guided-diffusion. We exclude the upsampling method from the comparison baseline in order to solely compare models synthesized in the same dimension. In this case, as drawing 1,281,167 samples from ADM is too expensive given our computational budget, we train our discriminator with 400,000 samples. Given our budget, it took nearly 1 day to train 2 epochs. In total, we train 10 epochs, and still we achieve SOTA performance with such a small training budget. Instead of PFODE, we sample data in the same way of DDPM (Ho et al., 2020).

Table 9 shows experimental results in the ImageNet dataset. Cases of (a), (c), and (e) demonstrate the efficacy of the discriminator guidance. Cases of (b) and (d-1,2) are for achieving the SOTA performance with the discriminator guidance. For (d-2), we multiply to DG weight by the norm ratio of the classifier guidance and the discriminator guidance, so to balance the guidance scale. Also, for the samples of density-ratio less than 0 in every odd denoising steps, we set  $w_{t< t_0}^{DG}$  by 0.75. Otherwise,  $w_{t< t_0}^{DG}=1$ . In (e), we apply Adaptive CG/DG to report the performance of ADM-G++. As in (d-2), 1/3 of (e) experiment represents that we boost the DG weight by a factor of 3 for samples of density-ratio less than 0 in every odd denoising steps.

Figure 23-(a) shows the IS-recall curve by discriminator training epochs. We fix all the other hyperparameters except the discriminator network. Figure 23-(a) illustrates that the discriminator guidance has an effect of increasing the recall metric, which implies that a well-trained discriminator facilitates a diverse generation. Due to the diverse generation, the IS metric is decreased. Similarly, Figure 23-(b) shows that ADM-G++ significantly improves the sample diversity with a sacrifice in the precision metric.

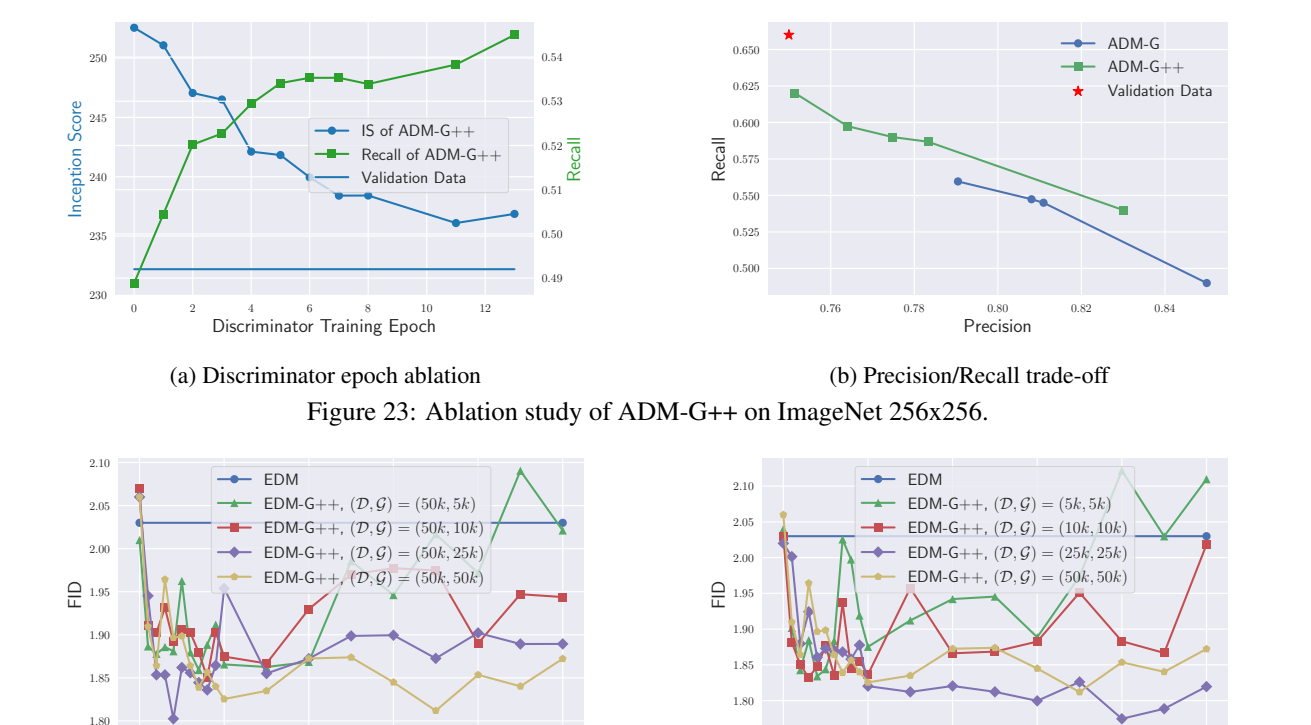


Figure 24: Study of EDM on CIFAR-10 with respect to the number of training data. (a) is the case with full real data  $\mathcal{D}$  and partial sample data  $\mathcal{G}$  and (b) is the case with partial  $\mathcal{D}$  and partial  $\mathcal{G}$ .

Discriminator Training Epochs

(b) Partial data and partial sample ablation

#### **D.2. More Ablation Studies**

#### D.2.1. DISCRIMINATOR TRAINING

Discriminator Training Epochs

(a) Full data and partial sample ablation

Ablation of # Training Data Figure 24 shows the ablation study on the number of training data on CIFAR-10. The discriminator guidance requires many samples from  $p_{\theta_{\infty}}$  to learn the density-ratio, so this could arise the computational issue in some cases. For that, we train the discriminator with the full set of real data and a partial set of sample data in Figure 24-(a). In other words, the case of  $(\mathcal{D},\mathcal{G})=(50k,25k)$  represents for the case of the full use of real data as  $\mathcal{D}$  and the half number of sample data as  $\mathcal{G}$  in Algorithm 1. Figure 24-(b), on the other hand, uses the same number of real data for discriminator training. For both experiments, the discriminator suffers from the overfitting issue as the number of generated data decreases.

Analogous to Figure 24-(a), Figure 24-(b) shows the another ablation study on the number of training data. The situation is a bit different: in this case, we also reduce the size of real data as well as the sample data. Comparing Figure 24-(b) with Figure 24-(a), it is generally not recommendable in any cases. The overfitting arises faster, leading the performance gets worsened faster.

**Ablation of** # **Batch Size** Figure 25-(a) illustrates the ablation study on the number of training batch size on CIFAR-10. Figure 25-(a) implies that the number of batch size is not a crucial factor for final performance of discriminator guidance.

Ablation of Temporal Weight  $\lambda$  Figure 25-(b) shows indistinguishable FID by the variance of temporal weighting function  $\lambda$  for  $\mathcal{L}_{\phi}$  of Eq. (5). We experiment with a uniform distribution  $\lambda(t) \propto 1$ , an importance-weighted (Song et al., 2021) distribution  $\lambda(t) = \frac{g^2(t)}{\sigma^2(t)}$  that is one of a common practice, and two  $\beta$ -related distributions of  $\lambda(t) = \sqrt{\beta(t)}$  and  $\lambda(t) = \beta(t)$ . We train the discriminator with LVP-SDE. Figure 25-(b) demonstrates that there is no significant difference between the choice of  $\lambda$ .

**Ablation of SDE** Figure 26-(a) empirically shows that using LVP-SDE as discriminator SDE performs better than using WVE-SDE. This indicates an important fact: while score training is beneficial with WVE-SDE, discriminator training best

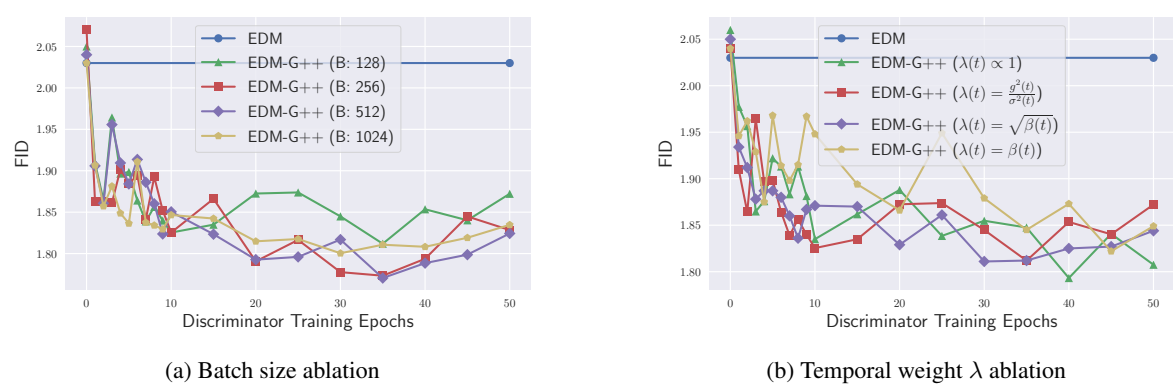


Figure 25: Study of EDM on CIFAR-10 with respect to (a) the number of training batch size and (b) the temporal weight  $\lambda$ .

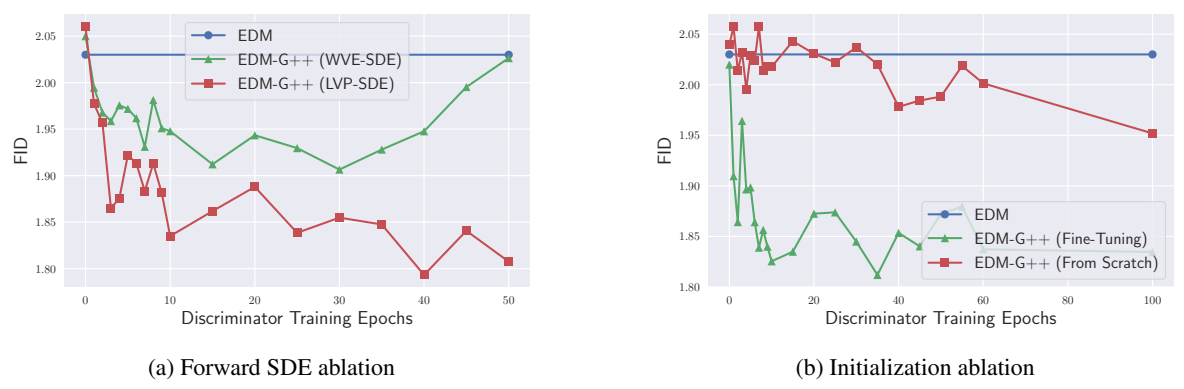


Figure 26: Study of EDM on CIFAR-10 with respect to (a) the discriminator diffusing method and (b) the discriminator parameter initialization.

fits with LVP-SDE. We, therefore, train the discriminator with LVP-SDE as default.

**Ablation of Parameter Initialization** Figure 26-(b) shows that the fine-tuning performs strictly better than the training from scratch. For the setting of fine-tuning, we fix the pre-trained classifier parameters, and only train the shallow U-Net for discriminator. In contrast, we train all the parameters including that of the latent extractor, and we set fine-tuning as default in our paper.

Additionally, we find that Exponential Moving Average (EMA) has nearly no effect on the discriminator training, and we do not apply EMA of our discriminator training.

#### D.2.2. AFTER DISCRIMINATOR TRAINING

Ablation of Discriminator Training in Latent Diffusion on CIFAR-10 Figure 27 additionally studies LSGM on CIFAR-10. Figure 27 shows FID by discriminator training. The performance saturates after nearly 300 epochs, and it is because we do not use a pre-trained latent extractor for LSGM. Kim et al. (2022a) clarify that latent diffusion models in general have no diffusion process in the pixel space as long as models use auto-encoder structure to map data to latent. We could detour this problem by defining the diffused data as a decoded diffused latent  $\mathbf{x}_t = Dec(\mathbf{z}_t)$ , but there is no pre-trained classifier for generic diffusion strategy nor latent diffusion space. We leave it as future work in this direction. In our implementation, we train a U-Net encoder from scratch. This takes a long time to saturate, but FID improves immediately after the discriminator training.

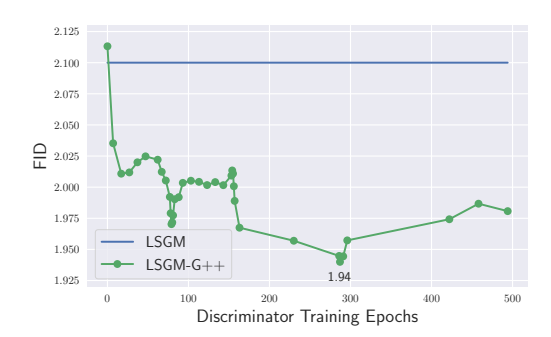
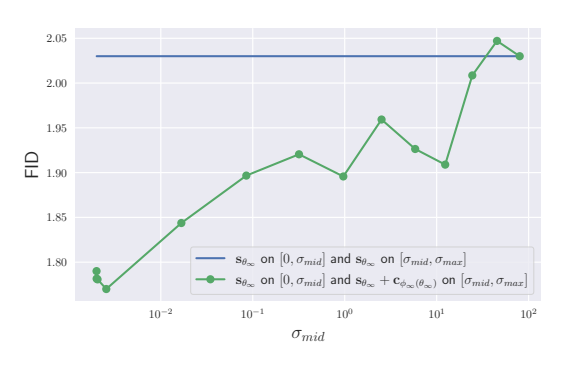
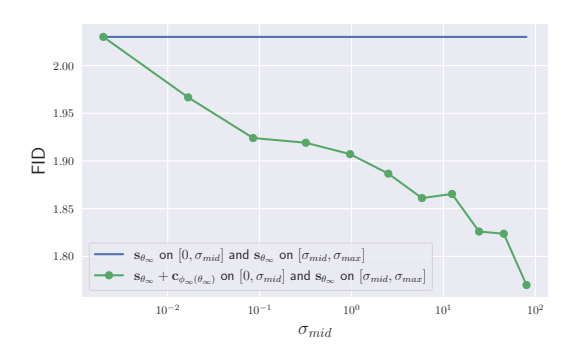


Figure 27: Discriminator epoch ablation.

Ablation of optimal scales on CIFAR-10 Figure 28 studies the minimum/maximum diffusion scales to apply DG. For the





(a) Minimum DG scale ablation

(b) Maximum DG scale ablation

Figure 28: Study of EDM on CIFAR-10 for optimal scales to apply DG: (a) minimum scale, (b) maximum scale.

experiment in Figure 28-(a), we divide the diffusion scales by  $\sigma_{mid}$ , and denoise with the reverse-time generative process

$$d\mathbf{x}_t = \left[\mathbf{f}(\mathbf{x}_t, t) - g^2(t)(\mathbf{s}_{\theta_{\infty}} + \mathbf{c}_{\phi_{\infty}})(\mathbf{x}_t, t)\right] d\bar{t} + g(t) d\bar{\mathbf{w}}_t,$$

on the large range  $[\sigma_{mid}, \sigma_{max}]$ , and denoise with

$$d\mathbf{x}_t = \left[ \mathbf{f}(\mathbf{x}_t, t) - g^2(t) \mathbf{s}_{\boldsymbol{\theta}_{\infty}}(\mathbf{x}_t, t) \right] d\bar{t} + g(t) d\bar{\mathbf{w}}_t,$$

on the small range  $[0, \sigma_{mid}]$ . With this ablation study, we could find the optimal minimum stopping scale to apply the diffusion scale. Figure 28-(a) illustrates that the optimal stopping scale near  $\sigma_{mid}^* = 0.0025$ . This strictly positive optimal scale implies that either the score adjustment becomes inaccurate or the discretization error matters at the range of extremely low scale. In the density-ratio community, *density-chasm problem* is a well-known problem (Rhodes et al., 2020; Kato & Teshima, 2021) that depicts a poor density-ratio estimation when the two densities have distinctive supports. It arises from the training-test mismatch: the discriminator perfectly classifies real/fake, but the middle area between the real data support and the fake data support remain unoptimized. Therefore, the density-chasm problem is one of the reason for such a strictly positive optimal scale.

Figure 28-(b) studies the maximum diffusion scale to apply DG. Analogous to the experimental setting of Figure 28-(a), we divide the diffusion scales by  $\sigma_{mid}$ , and denoise with the reverse-time generative process

$$d\mathbf{x}_t = \left[\mathbf{f}(\mathbf{x}_t, t) - g^2(t)\mathbf{s}_{\boldsymbol{\theta}_{\infty}}(\mathbf{x}_t, t)\right] d\bar{t} + g(t) d\bar{\mathbf{w}}_t,$$

on the large range  $[\sigma_{mid}, \sigma_{max}]$ , and denoise with

$$d\mathbf{x}_t = \left[\mathbf{f}(\mathbf{x}_t, t) - g^2(t)(\mathbf{s}_{\theta_{\infty}} + \mathbf{c}_{\phi_{\infty}})(\mathbf{x}_t, t)\right] d\bar{t} + g(t) d\bar{\mathbf{w}}_t,$$

on the small range  $[0, \sigma_{mid}]$ . Contrastive to the minimum scale ablation study, the larger the scale DG applied, the better the performance. This means that the actual effect of DG lies in constructing the global shape of the generation, rather than denoising fine-details. In the community of diffusion models, there are only a few works that systematically divide the context generation ability and fine-detail capturing ability of diffusion models. Figure 28 clarify that DG effectively adjusts the context generation ability of diffusion models, rather than cleansing the fine-dust in images.

**Ablation of NFE on FFHQ** Figure 29 illustrates FID by NFE after discriminator training. For visualization purpose, we select the best hyperparameters to experiment with, except NFE. Similar to NFE ablation on CIFAR-10, the discriminator guidance keeps enhancing FID throughout NFEs.

## **D.3. Uncurated Samples**

Figures 30, 31, 32, 33, 34, 35, 36 compare ADM-G++ (cfg=0.10) with the vanilla ADM to illustrate how sample fidelity is improved while keeping the sample diversity. ADM-G++ (cfg=0.10) performs FID of 4.45 and recall of 0.60, and ADM performs FID of 10.94 and recall of 0.63.

Figures 37, 38, 39, 40, 41, 42, 43 compare ADM-G++ (cfg=0.75) with ADM-G (cfg=1.50). These figures show the discriminator guidance is effective in high-dimensional dataset.

Figures 44, 45, 46, 47, and 48 show uncurated samples from unconditional CIFAR-10 with LSGM-G++, unconditional CIFAR-10 with EDM-G++, conditional CIFAR-10 with EDM-G++, unconditional CelebA with STDDPM-G++, and unconditional FFHQ with EDM-G++.

Figure 49 shows the uncurated samples from I2I translation task.

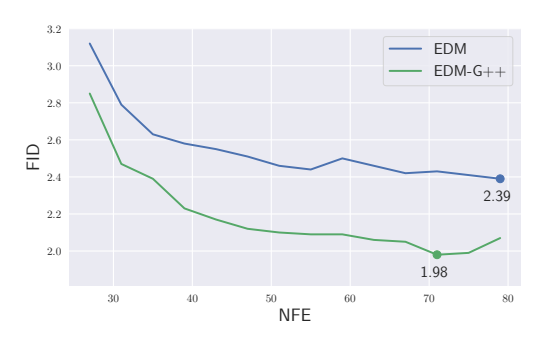


Figure 29: NFE ablation on FFHQ.

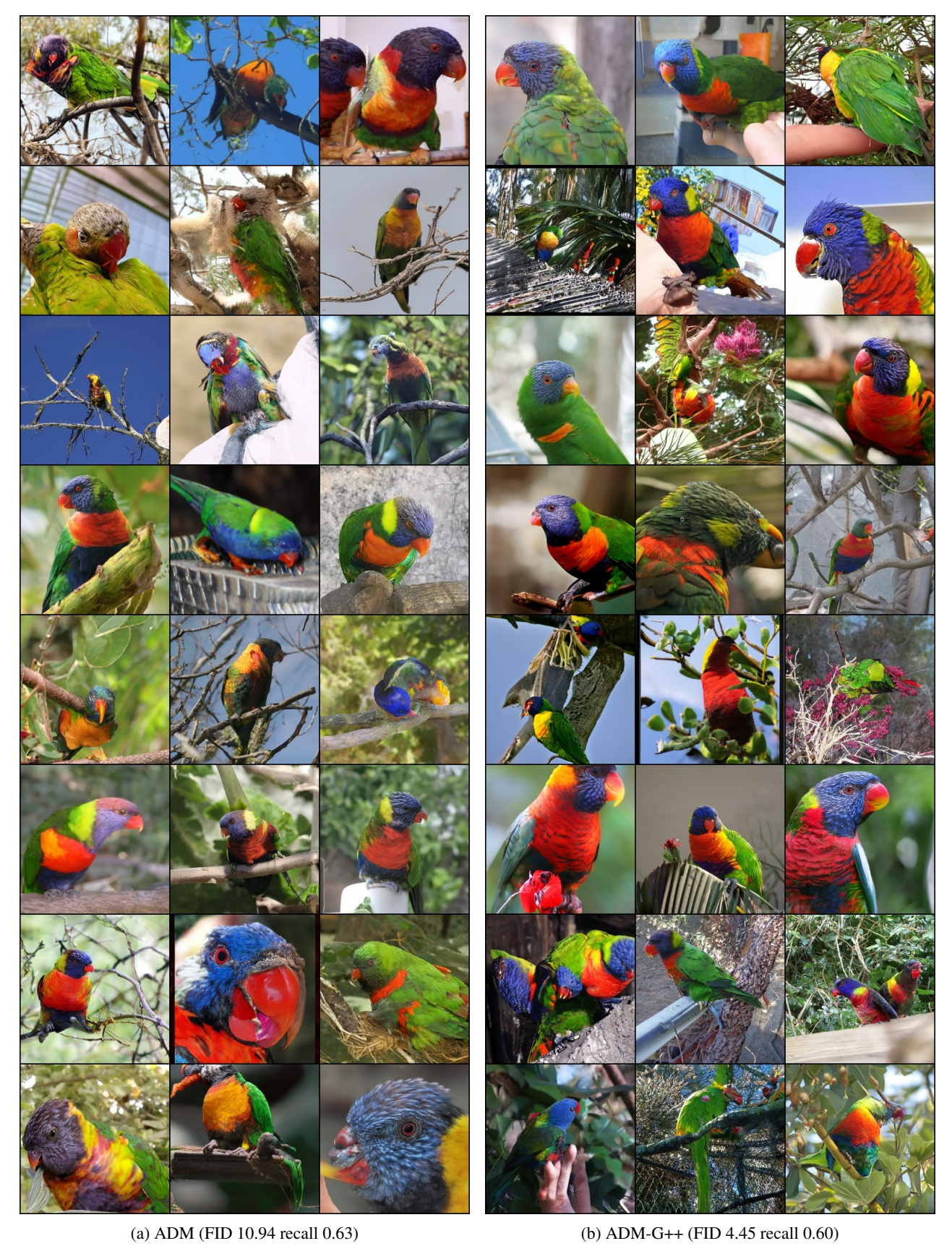


Figure 30: Uncurated random samples from lorikeet class (90) (a) ADM with poor FID (10.94) and good recall (0.63), (b) ADM-G++ with good FID (4.45) and good recall (0.60).



Figure 31: Uncurated random samples from flamingo class (130) (a) ADM with poor FID (10.94) and good recall (0.63), (b) ADM-G++ with good FID (4.45) and good recall (0.60).

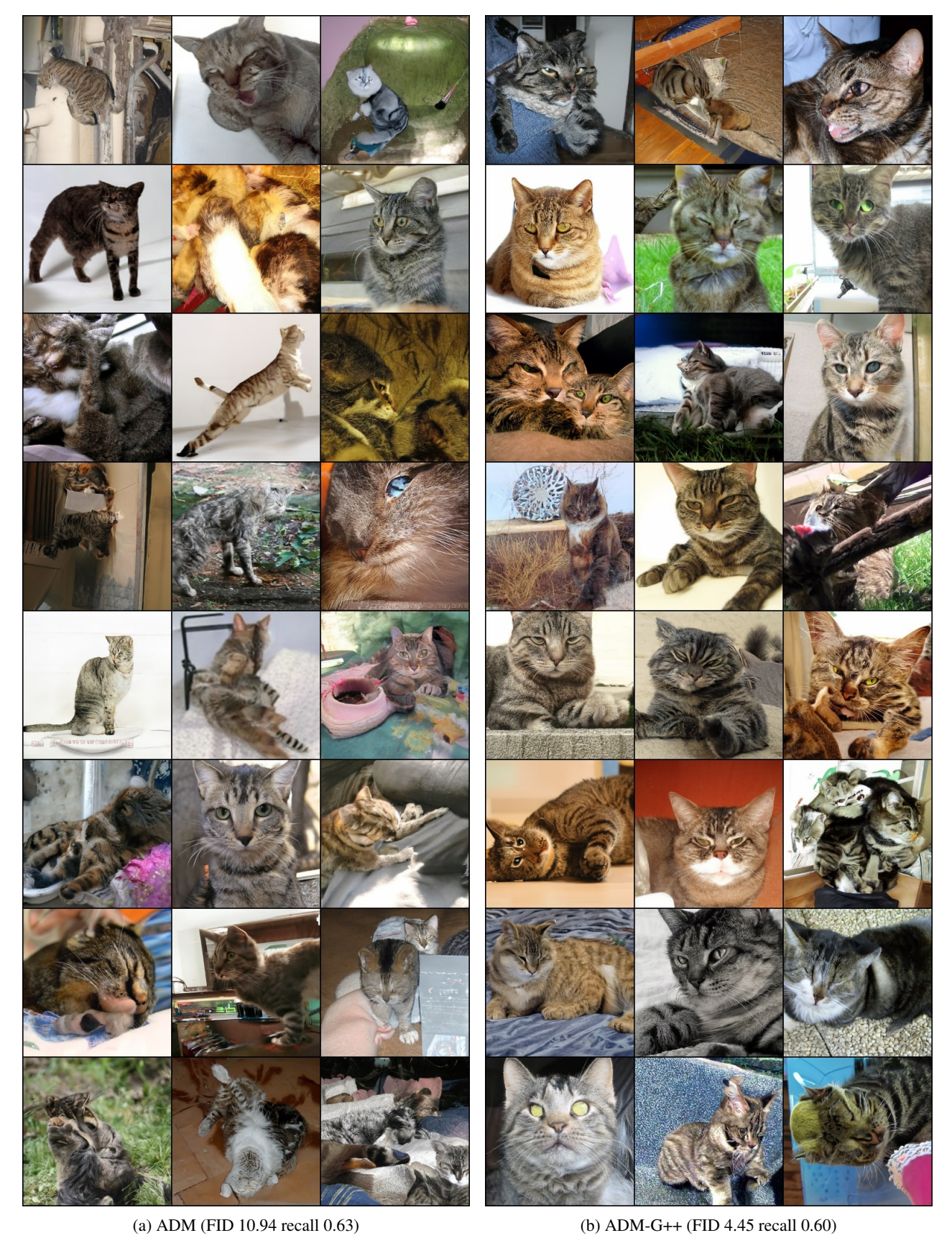


Figure 32: Uncurated random samples from tabby cat class (281) (a) ADM with poor FID (10.94) and good recall (0.63), (b) ADM-G++ with good FID (4.45) and good recall (0.60).



Figure 33: Uncurated random samples from monarch butterfly class (323) (a) ADM with poor FID (10.94) and good recall (0.63), (b) ADM-G++ with good FID (4.45) and good recall (0.60).



Figure 34: Uncurated random samples from african elephant class (386) (a) ADM with poor FID (10.94) and good recall (0.63), (b) ADM-G++ with good FID (4.45) and good recall (0.60).

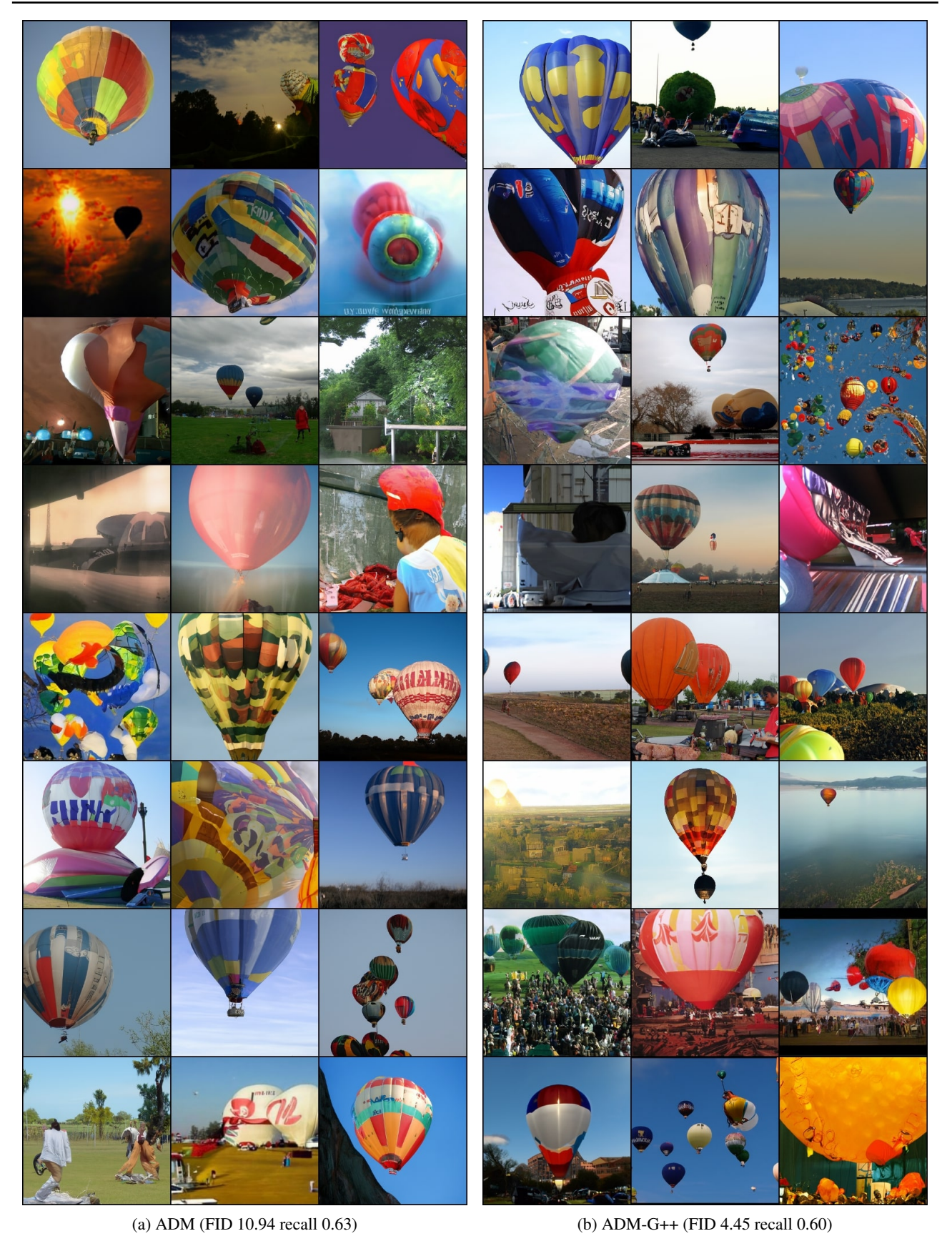


Figure 35: Uncurated random samples from ballon class (417) (a) ADM with poor FID (10.94) and good recall (0.63), (b) ADM-G++ with good FID (4.45) and good recall (0.60).



Figure 36: Uncurated random samples from fountain class (562) (a) ADM with poor FID (10.94) and good recall (0.63), (b) ADM-G++ with good FID (4.45) and good recall (0.60).

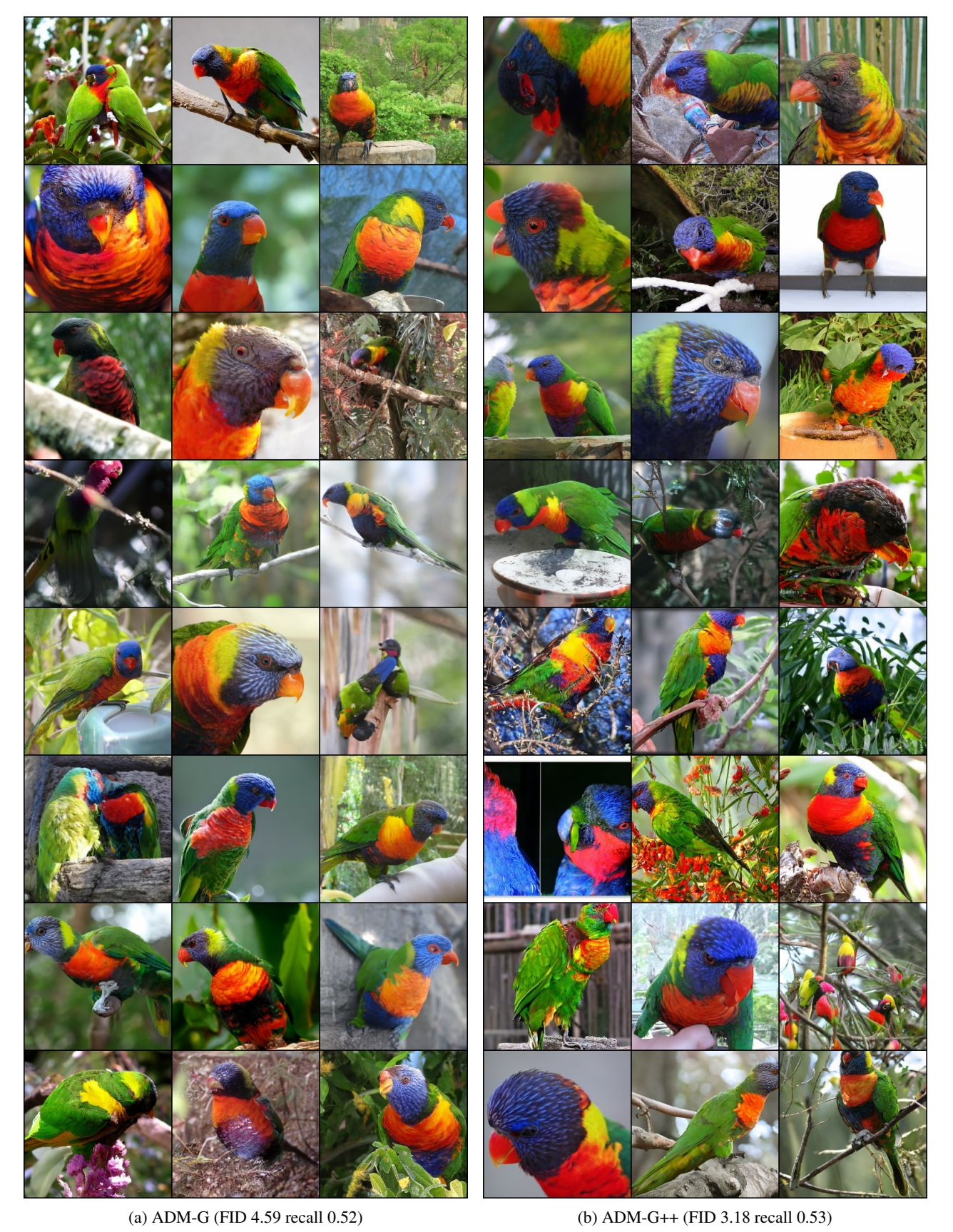


Figure 37: Uncurated random samples from lorikeet class (90) (a) ADM-G with good FID (4.59) and poor recall (0.52), (b) ADM-G++ with SOTA FID (3.18) and moderate recall (0.53).



Figure 38: Uncurated random samples from flamingo class (130) (a) ADM-G with good FID (4.59) and poor recall (0.52), (b) ADM-G++ with SOTA FID (3.18) and moderate recall (0.53).

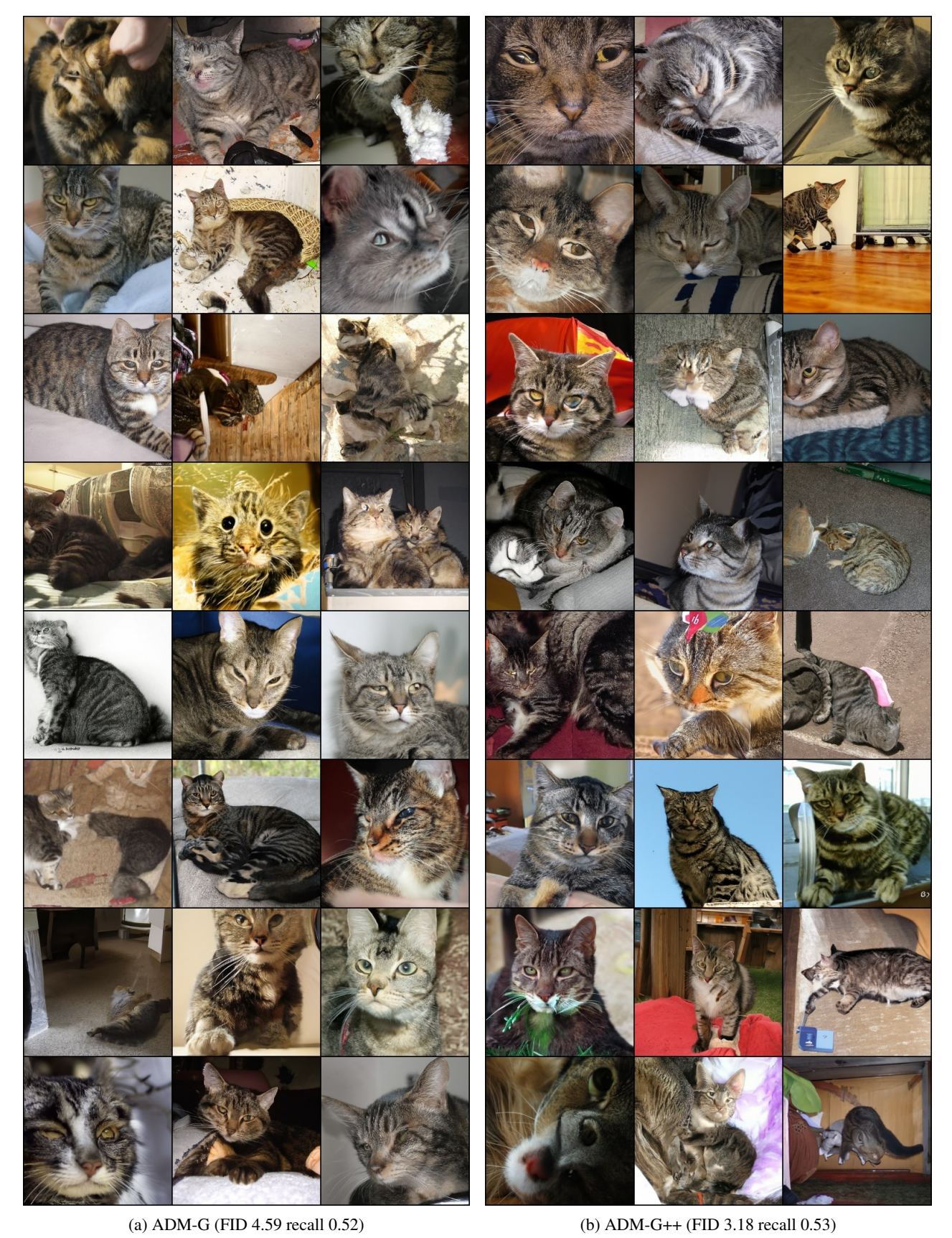


Figure 39: Uncurated random samples from tabby cat class (281) (a) ADM-G with good FID (4.59) and poor recall (0.52), (b) ADM-G++ with SOTA FID (3.18) and moderate recall (0.53).

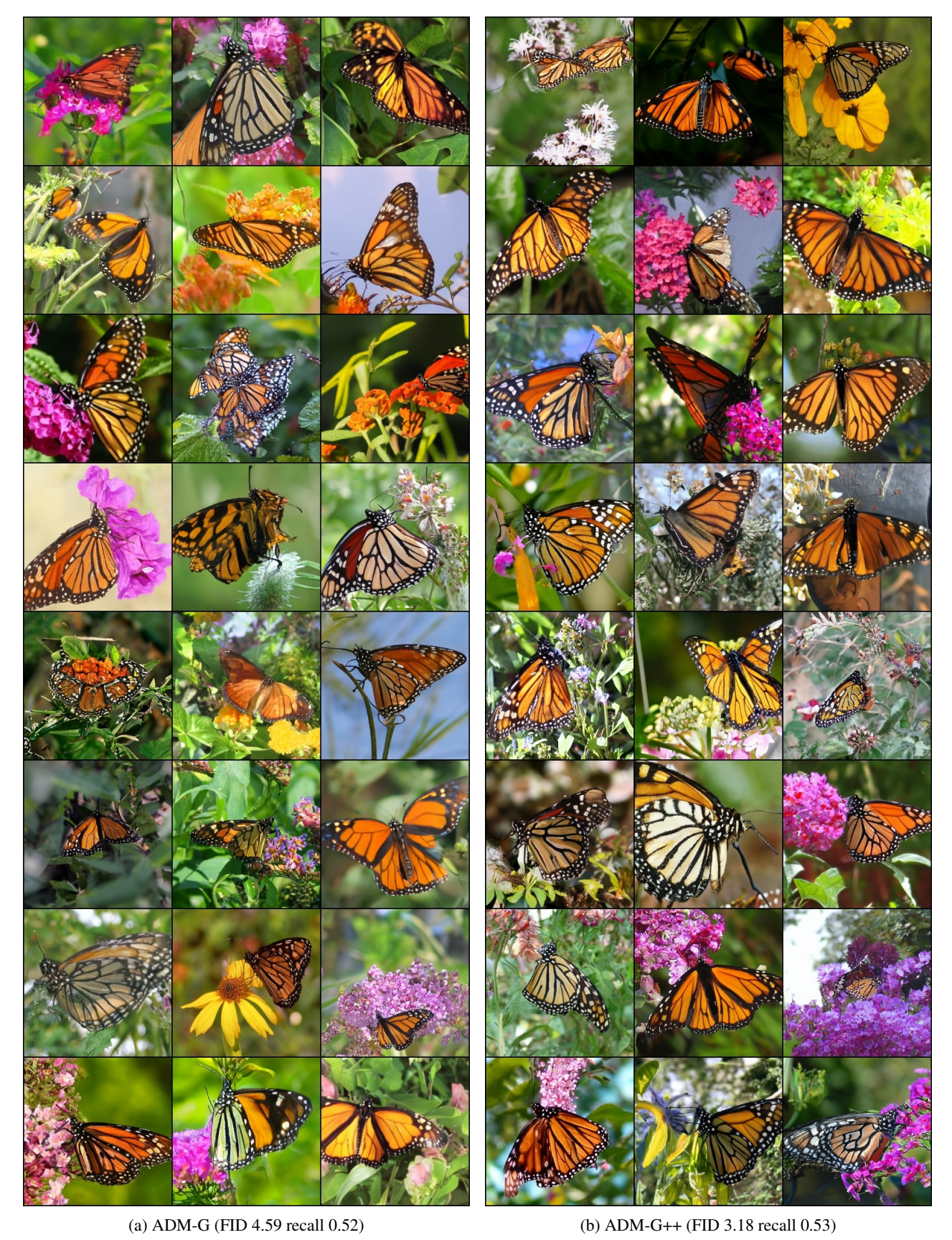


Figure 40: Uncurated random samples from monarch butterfly class (323) (a) ADM-G with good FID (4.59) and poor recall (0.52), (b) ADM-G++ with SOTA FID (3.18) and moderate recall (0.53).

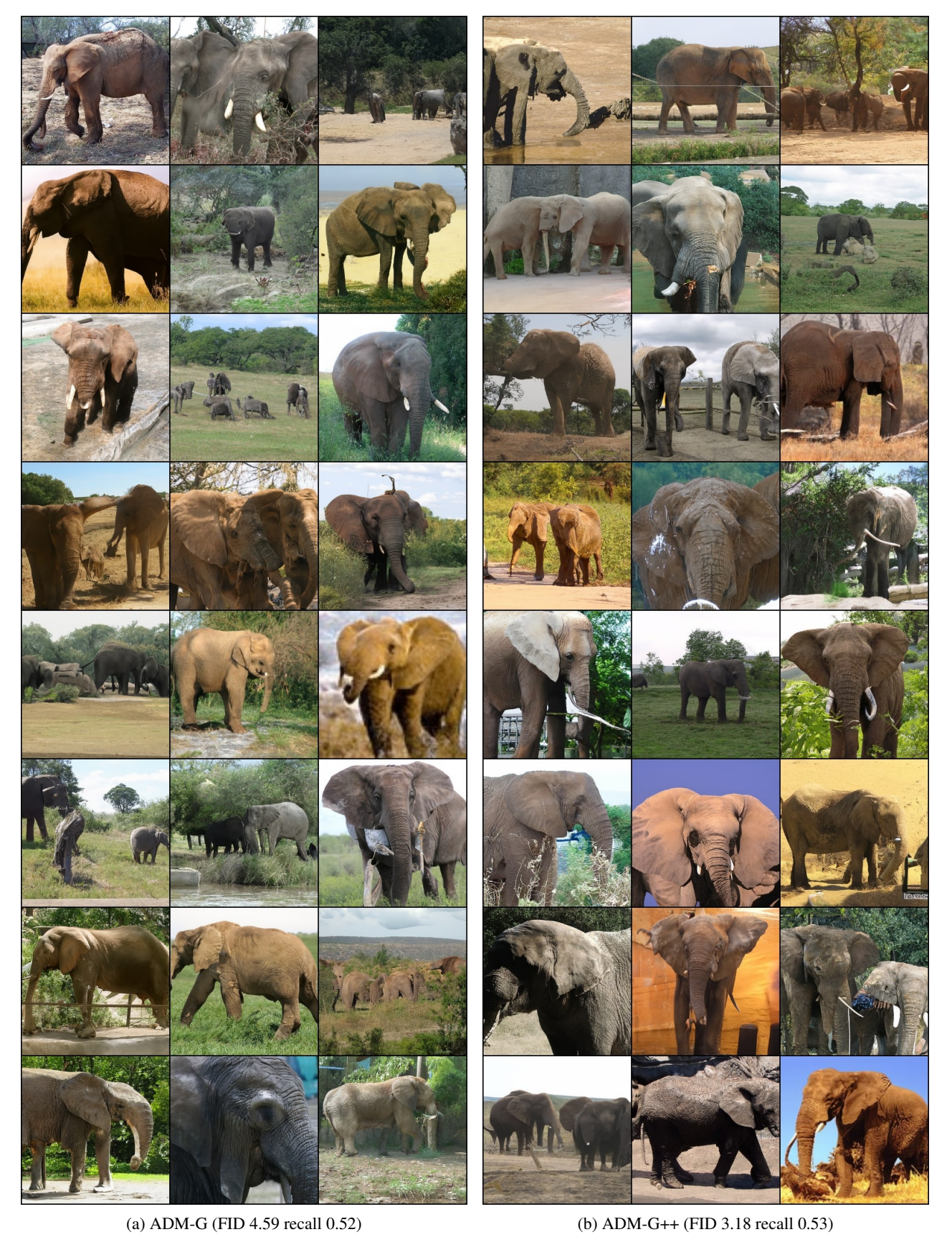


Figure 41: Uncurated random samples from african elephant class (386) (a) ADM-G with good FID (4.59) and poor recall (0.52), (b) ADM-G++ with SOTA FID (3.18) and moderate recall (0.53).



Figure 42: Uncurated random samples from ballon class (417) (a) ADM-G with good FID (4.59) and poor recall (0.52), (b) ADM-G++ with SOTA FID (3.18) and moderate recall (0.53).

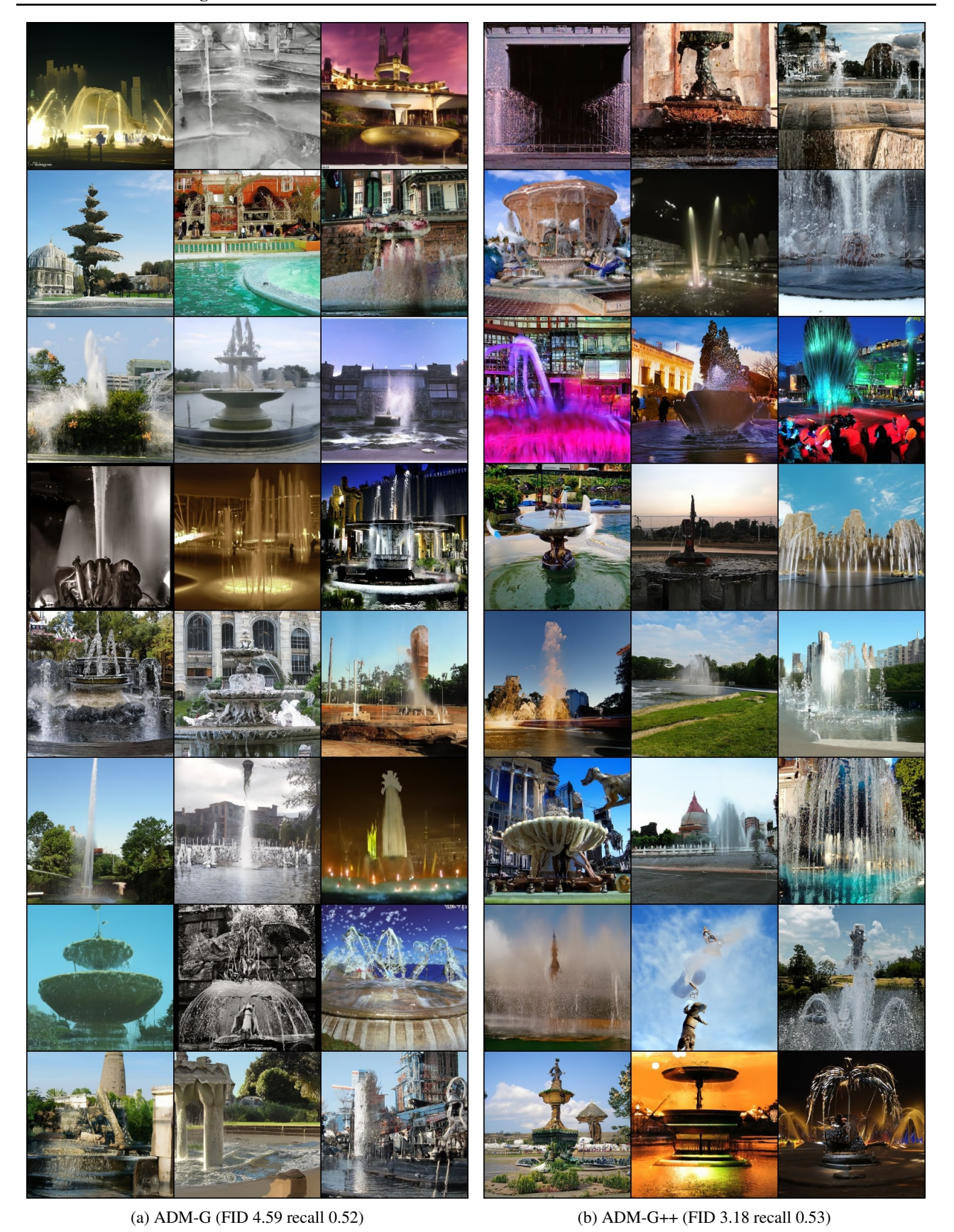


Figure 43: Uncurated random samples from fountain class (562) (a) ADM-G with good FID (4.59) and poor recall (0.52), (b) ADM-G++ with SOTA FID (3.18) and moderate recall (0.53).

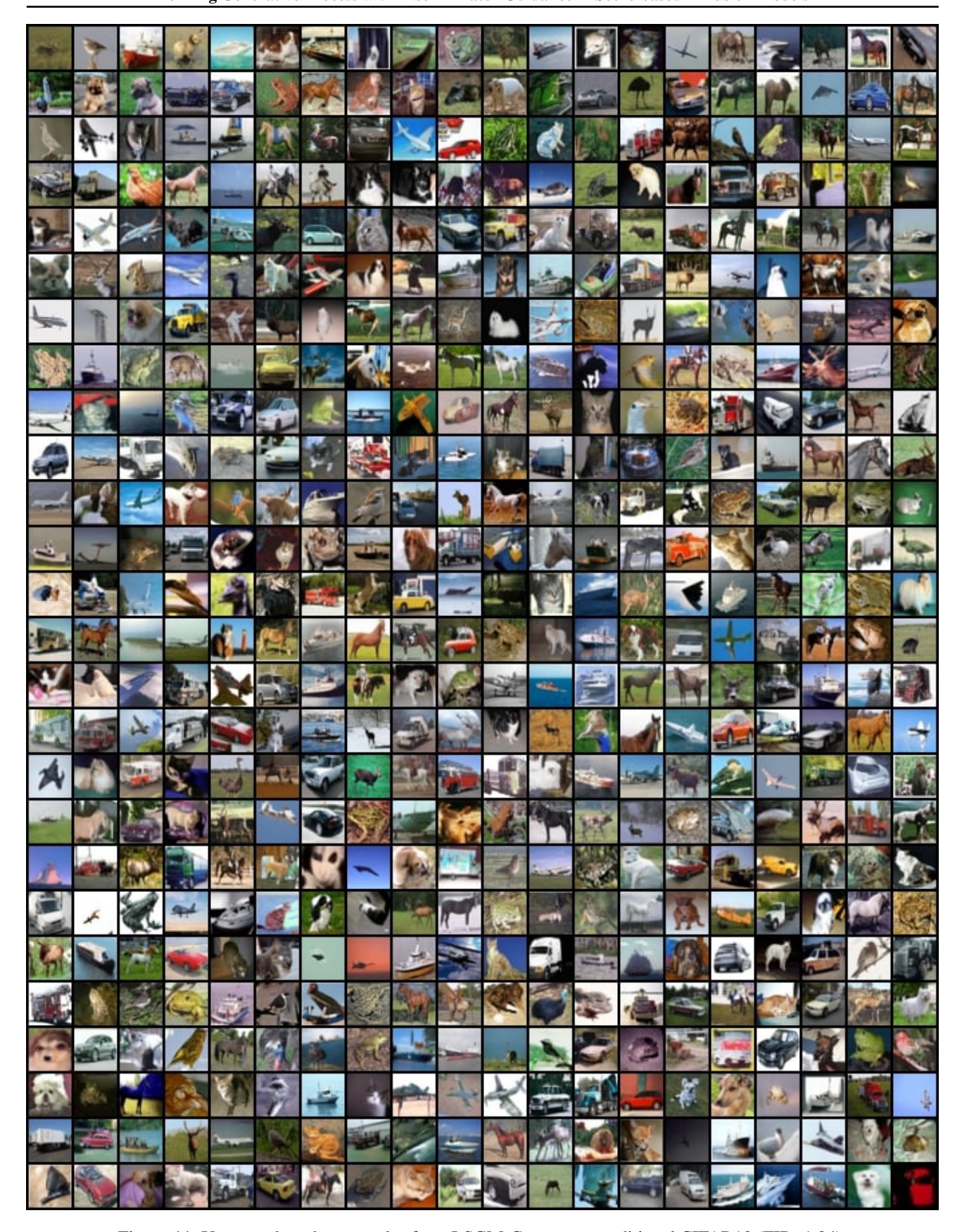


Figure 44: Uncurated random samples from LSGM-G++ on unconditional CIFAR10 (FID: 1.94).



Figure 45: Uncurated random samples from EDM-G++ on unconditional CIFAR10 (FID: 1.77).

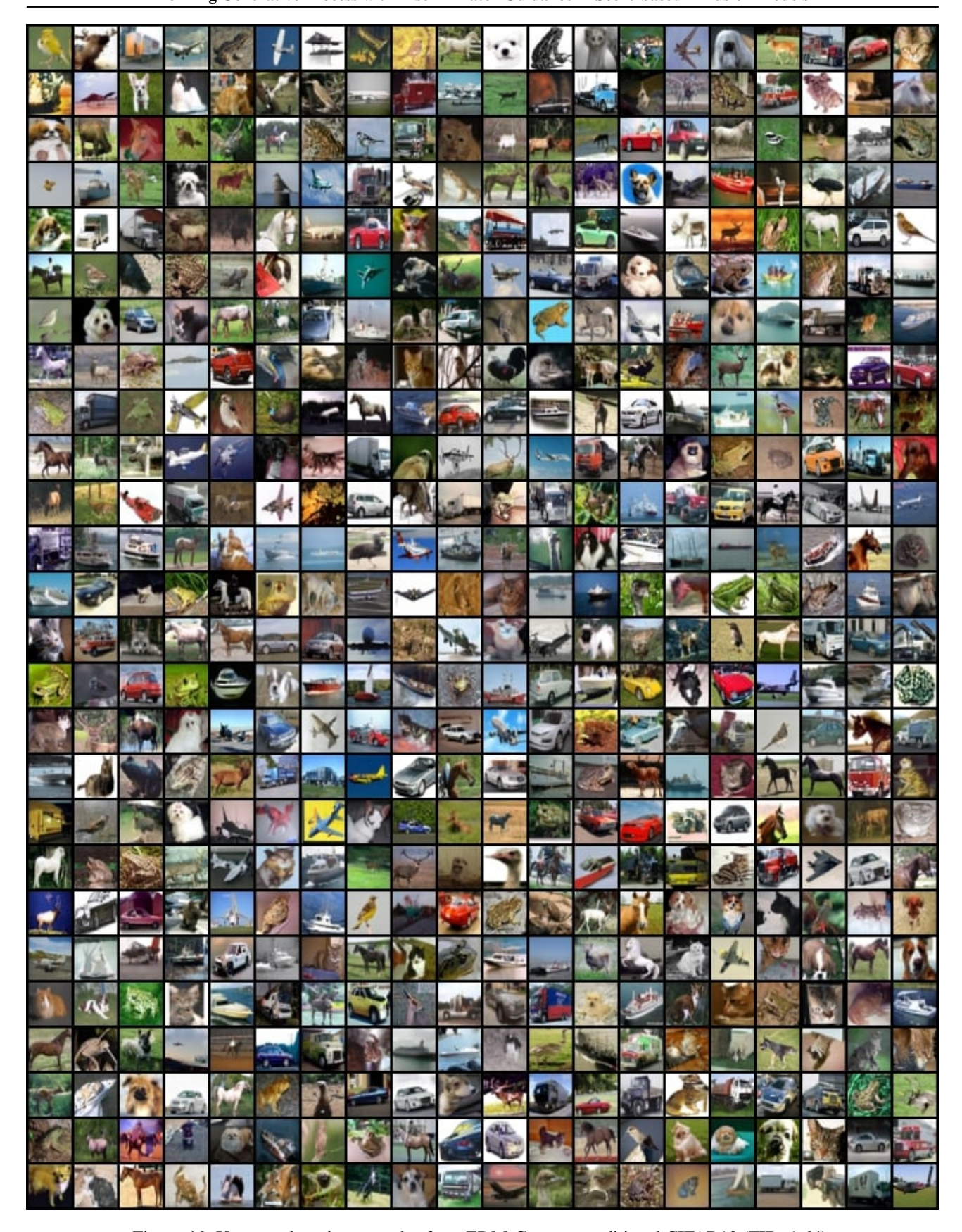


Figure 46: Uncurated random samples from EDM-G++ on conditional CIFAR10 (FID: 1.64).

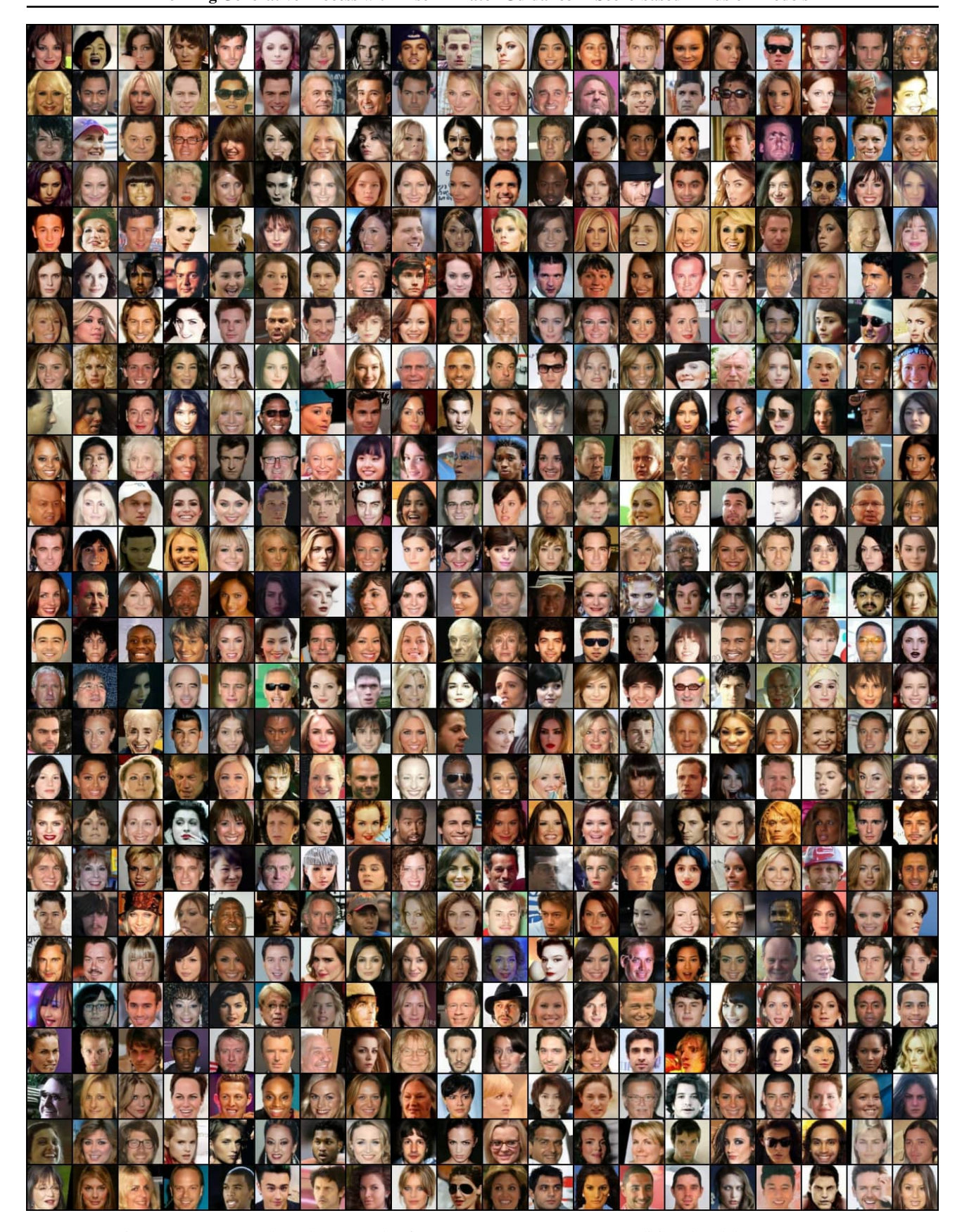


Figure 47: Uncurated random samples from STDDPM-G++ on unconditional CelebA (FID: 1.34).

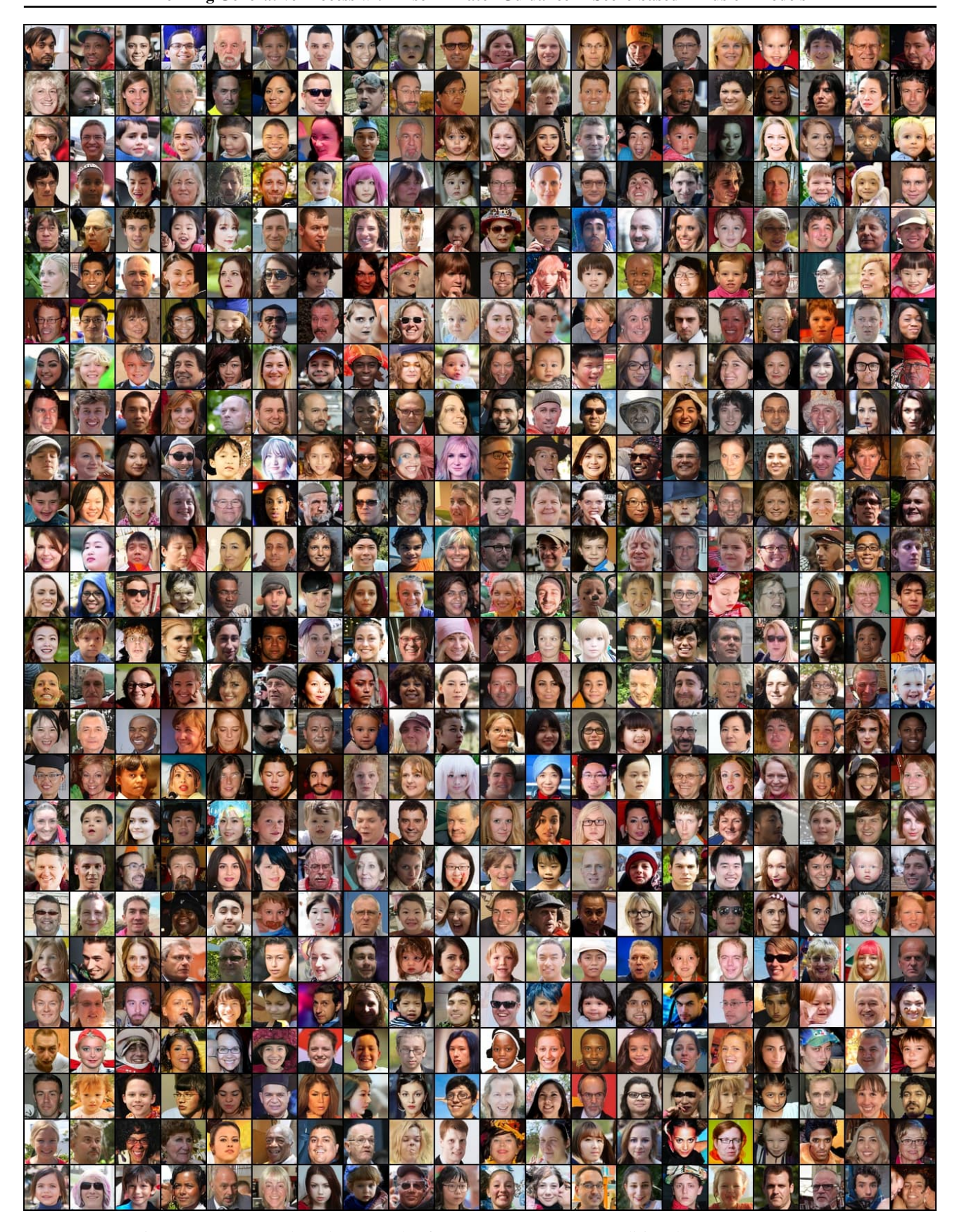


Figure 48: Uncurated random samples from EDM-G++ on unconditional FFHQ (FID: 1.98).



Figure 49: Uncurated random translated samples from (a) source cat, (b) SDEdit (FID: 74.02, L2: 49.22, PSNR: 19.21, SSIM: 0.42), and (c) SDEdit + DG with  $w_t^{DG}=8$  (FID: 61.92, L2: 50.62, PSNR: 18.94, SSIM: 0.41).